

1   **Title:** Integrating genetic regulation and single-cell expression with GWAS prioritizes causal genes  
2   and cell types for glaucoma

3  
4   **Authors:**  
5   Andrew R. Hamel<sup>1,2,3</sup>, Wenjun Yan<sup>4,\*</sup>, John M. Rouhana<sup>1,2,3,\*</sup>, Aboozar Monovarfeshani<sup>4,\*</sup>, Xinyi  
6   Jiang<sup>5,6</sup>, Puja A. Mehta<sup>1,2,3</sup>, Jayshree Advani<sup>7</sup>, Yuyang Luo<sup>1,2,3</sup>, Qingnan Liang<sup>8</sup>, Skanda  
7   Rajasundaram<sup>2,9,10</sup>, Arushi Shrivastava<sup>1,2,3</sup>, Katherine Duchinski<sup>1,2,3</sup>, Sreekar Mantena<sup>1,11</sup>, Jiali  
8   Wang<sup>1,2,3</sup>, Tavé van Zyl<sup>4,12</sup>, Louis R. Pasquale<sup>13</sup>, Anand Swaroop<sup>7</sup>, Puya Gharahkhani<sup>14</sup>, Anthony  
9   P. Khawaja<sup>15</sup>, Stuart MacGregor<sup>14</sup>, International Glaucoma Genetics Consortium (IGGC), Rui  
10   Chen<sup>8</sup>, Veronique Vitart<sup>5</sup>, Joshua R. Sanes<sup>4</sup>, Janey L. Wiggs<sup>1,2,3</sup>, Ayellet V. Segrè<sup>1,2,3,#</sup>

11  
12   **Affiliations:**  
13   <sup>1</sup>Ocular Genomics Institute, Department of Ophthalmology, Massachusetts Eye and Ear, Boston, MA  
14   <sup>2</sup>Department of Ophthalmology, Harvard Medical School, Boston, MA  
15   <sup>3</sup>Broad Institute of Harvard and MIT, Cambridge, MA.  
16   <sup>4</sup>Department of Molecular and Cellular Biology and Center for Brain Science, Harvard University,  
17   Cambridge, MA, USA

18   <sup>5</sup>MRC Human Genetics Unit, Institute of Genetics and Cancer, The University of Edinburgh, Edinburgh,  
19   UK

20   <sup>6</sup>Centre for Genomic and Experimental Medicine, Institute of Genetics and Molecular Medicine, The  
21   University of Edinburgh, Edinburgh, UK

22   <sup>7</sup>Neurobiology, Neurodegeneration and Repair Laboratory, National Eye Institute, National Institutes of  
23   Health, Bethesda, Maryland, USA

24   <sup>8</sup>Department of Molecular and Human Genetics, Baylor College of Medicine, TX

25   <sup>9</sup>Centre for Evidence-Based Medicine, University of Oxford, Oxford, UK

26   <sup>10</sup>Faculty of Medicine, Imperial College London, London, UK

27   <sup>11</sup>Harvard/MIT MD-PhD Program, Harvard Medical School, Boston, MA

28   <sup>12</sup>Department of Ophthalmology and Visual Sciences, Yale School of Medicine, New Haven, CT

29   <sup>13</sup>Department of Ophthalmology, Icahn School of Medicine at Mount Sinai, New York, NY, USA

30   <sup>14</sup>QIMR Berghofer Medical Research Institute, Brisbane, Queensland, 4029, Australia

31   <sup>15</sup>NIHR Biomedical Research Centre, Moorfields Eye Hospital NHS Foundation Trust and UCL  
32   Institute of Ophthalmology, London, UK

33   \* Co-second authors, these authors contributed equally

34   # Correspondence to be addressed to Ayellet V. Segrè: [ayellet\\_segre@meei.harvard.edu](mailto:ayellet_segre@meei.harvard.edu)

35

36 **Abstract**

37  
38 Primary open-angle glaucoma (POAG), characterized by retinal ganglion cell death, is a leading  
39 cause of irreversible blindness worldwide; however, the molecular and cellular causes are not well  
40 understood. Elevated intraocular pressure (IOP) is a major risk factor, but many patients have  
41 normal IOP. Colocalization and Mendelian randomization analysis of >240 POAG and IOP GWAS  
42 loci and of overlapping eQTLs and sQTLs in 49 GTEx tissues and retina prioritized causal genes  
43 for 60% of loci. These genes were enriched in pathways implicated in extracellular matrix  
44 organization, cell adhesion, and vascular development. Analysis of single-nucleus RNA-seq of  
45 glaucoma-relevant eye tissues revealed that the colocalizing genes and genome-wide POAG and  
46 IOP associations were enriched in specific cell types in the aqueous outflow pathways, retina, optic  
47 nerve head, peripapillary sclera, and choroid. This study nominated IOP-dependent and  
48 independent regulatory mechanisms, genes, and cell types that may contribute to POAG  
49 pathogenesis.

50

51 **Introduction**

52  
53 Primary open-angle glaucoma (POAG) is the leading cause of irreversible blindness  
54 worldwide among people over the age of 55<sup>1</sup>. It is characterized by progressive optic neuropathy,  
55 caused by the gradual death of retinal ganglion cells (RGCs) that transmit visual information from  
56 the outer retina to the brain via the optic nerve (myelinated RGC axons)<sup>2</sup>. Elevated intraocular  
57 pressure (IOP) is a major risk factor for POAG<sup>3</sup> and is primarily caused by decreased outflow of the  
58 aqueous humor from the ocular anterior segment. Decreased outflow may be due to abnormal  
59 function of structures in the anterior segment of the eye, consisting of the trabecular meshwork  
60 (TM)<sup>4</sup> and Schlemm's canal (SC)<sup>5</sup> in the conventional outflow pathway, and the ciliary muscle and  
61 iris in the uveoscleral (unconventional) pathway<sup>6</sup>. However, about one third of patients with POAG  
62 display optic nerve degeneration in the absence of abnormally high IOP measurements (normal  
63 tension glaucoma (NTG))<sup>7</sup>. Conversely, many people with elevated IOP do not develop glaucoma,  
64 suggesting that other processes, including increased RGC susceptibility to normal IOP, might also  
65 lead to optic nerve damage. Currently, neuroprotective therapies are lacking, and medications that  
66 reduce IOP have limited effectiveness<sup>2</sup>. Gaining a better understanding of the molecular and  
67 cellular causes of POAG in the anterior and posterior segments of the eye could suggest novel  
68 therapeutic targets.

69 A recent multi-ethnic genome-wide association study (GWAS) meta-analysis of 34,179  
70 POAG cases and 349,321 controls of European, Asian, and African ancestries identified 127 risk  
71 loci associated with POAG<sup>8</sup>, explaining ~9% of POAG heritability, and a meta-analysis of the  
72 European subset identified 68 POAG loci<sup>8</sup>, some of which were not uncovered in the cross-ancestry  
73 meta-analysis. Furthermore, a GWAS meta-analysis of IOP performed on 139,555 individuals,  
74 primarily of European descendant<sup>9</sup>, has identified 133 independent associations in 112 loci, largely  
75 overlapping with two other studies<sup>10,11</sup>. The IOP variants' effect sizes and direction of effect are  
76 highly correlated with their effect on POAG risk<sup>8,9</sup>, and together they explain 9-17% of IOP  
77 heritability. Vertical-cup-to-disc ratio (VCDR), central corneal thickness, and corneal hysteresis, a  
78 measure of the viscoelastic damping of the cornea, have also been associated with POAG risk,  
79 and large GWAS meta-analyses have uncovered 70-200 genetic associations for these traits<sup>12-23</sup>.

80 Identifying putative causal genes and cell types underlying the genetic associations with  
81 POAG and its related traits is challenging. As with other complex traits, a majority of associated  
82 variants lie in noncoding regions and are enriched for regulatory effects<sup>24-26</sup>. Due to linkage  
83 disequilibrium (LD), the discovered associations typically tag multiple variants and genes, making  
84 it hard to pinpoint the implicated causal gene(s) from sequence alone. Furthermore, genetic  
85 regulatory effects in relevant ocular tissues are limited, reported to date only in retinal tissues<sup>27-30</sup>,  
86 and have not yet been detected at cellular resolution in other parts of the eye. Nevertheless, through  
87 single-cell or single-nucleus RNA-sequencing (sc/snRNA-seq), human cell atlases and cellular  
88 level transcriptomes have been generated for various non-diseased eye tissues relevant to POAG  
89 pathogenesis, including retina<sup>31-33</sup>, the aqueous humor outflow pathways<sup>34,35</sup>, six tissues in the  
90 anterior chamber<sup>36</sup>, and the optic nerve head (ONH), where RGCs pass to exit the eye, the optic  
91 nerve, and surrounding posterior tissues<sup>37</sup>. Using a method we recently developed, ECLIPSER<sup>38,39</sup>,  
92 we show that cell type-specific enrichment of genes mapped to GWAS loci of complex diseases  
93 and traits can help identify cell types of action for diseases in relevant tissues<sup>38,39</sup>.

94 In this study, we have combined expression quantitative trait loci (eQTLs) and splicing QTLs  
95 (sQTLs) in 49 (non-ocular) tissues from the Genotype-Tissue Expression (GTEx) Project<sup>26</sup>, retinal  
96 eQTLs<sup>31,32</sup>, retinal Hi-C data<sup>40</sup>, and single-cell expression from glaucoma-relevant eye tissues<sup>33,36,37</sup>  
97 with POAG and IOP genetic associations to identify regulatory mechanisms, genes, pathways, and  
98 cell types that may play an important role in POAG etiology.

## 99 **Results**

100 An overview of the analytical steps and approaches taken are described in Fig. 1 and  
101 Supplementary Note.

102

103 **POAG and IOP associations enriched among eQTLs and sQTLs.** To assess the relevance of  
104 eQTLs and sQTLs to POAG risk and IOP variation, we tested whether *cis*-eQTLs and *cis*-sQTLs  
105 (e/sQTLs) from 49 GTEx (v8) tissues<sup>26</sup> and peripheral retina *cis*-eQTLs<sup>27,28</sup> were enriched for POAG  
106 or IOP associations (GWAS P<0.05) using *QTLEnrich*<sup>24,26</sup> that adjusts for confounding factors and  
107 tissue sample size (Methods and Fig. 1a). We found significant enrichment of multiple POAG and  
108 IOP associations (both genome-wide significant and subthreshold) among eQTLs and sQTLs in  
109 most of the 49 GTEx tissues and in retina (Bonferroni-corrected P<5x10<sup>-4</sup>) (Fig. 2a, b and  
110 Supplementary Tables 1-3). Many of the top enriched GTEx tissues contain cell types that may be  
111 pathogenic to glaucoma (Supplementary Note). The relative contribution of sQTLs to POAG and  
112 IOP, as measured by adjusted fold-enrichment and estimated true positive rate, was larger than  
113 the relative contribution of eQTLs to these traits (One-sided Wilcoxon rank sum test P<1.5x10<sup>-11</sup>  
114 and P<0.03, respectively; Supplementary Fig. 1a-c, and Supplementary Tables 1-3), as observed  
115 with other complex traits<sup>26</sup>. The absolute number of eQTLs proposed to contribute to POAG and  
116 IOP (average 258 to 606 per tissue) was 2-fold larger than that of sQTLs (average 124 to 320 per  
117 tissue), likely due to the larger discovery rate of eQTLs compared to sQTLs<sup>26</sup> (Supplementary Fig.  
118 1a-c and Supplementary Table 1). The target genes of eQTLs or sQTLs with top-ranked POAG or  
119 IOP GWAS p-values (P<0.05) were enriched in metabolic and cellular processes (Methods;  
120 Supplementary Tables 4-5; Supplementary Note).

121  
122 **Colocalization analysis of POAG and IOP GWAS loci with *cis*-e/sQTLs.** Given the widespread  
123 e/sQTL enrichment of POAG and IOP associations, we used the e/sQTLs in all 49 GTEx tissues  
124 and retina eQTLs to propose putative causal genes that may underlie genome-wide significant loci  
125 for these traits. We applied two colocalization methods, eCAVIAR<sup>41</sup> and *enloc*<sup>42</sup>, to 127 POAG loci  
126 from a large cross-ancestry GWAS meta-analysis<sup>8</sup>, 68 POAG loci from a European (EUR) subset  
127 meta-analysis<sup>8</sup> (POAG EUR), and 133 IOP loci from a primarily European GWAS meta-analysis<sup>9</sup>  
128 (IOP) (variant list in Supplementary Table 6; Methods and Fig. 1a), and any e/sQTLs that  
129 overlapped each GWAS locus LD interval (Methods). The results are presented per trait and  
130 colocalization method in Supplementary Tables 7-12 and summarized in Supplementary Table 13.  
131 We defined a “comprehensive set” of putative causal genes and regulatory mechanisms for POAG  
132 and IOP as those e/sGenes that were significant with at least one of the colocalization methods  
133 (Colocalization posterior probability (CLPP) > 0.01 for eCAVIAR, and regional colocalization  
134 probability (RCP) > 0.1 for *enloc* (see Methods; Supplementary Table 13), filtering out potential  
135 false positives (See Methods and examples in Supplementary Fig. 3). The largest number of  
136 colocalizing e/sGenes was found in tibial nerve, adipose, skin, artery, and fibroblasts, among other

137 tissues, many of which contain cell types relevant to the pathogenicity of glaucoma (Supplementary  
138 Fig. 4). Eighteen retina eQTLs colocalized with 13 POAG and/or IOP loci (Column AH in  
139 Supplementary Table 13). The number of significantly colocalizing e/sGenes per tissue significantly  
140 correlated with tissue sample size (Pearson's  $R^2=0.72$ ,  $P=1\times10^{-14}$ , Supplementary Fig. 4) that is  
141 also associated with the number of detected e/sQTLs per tissue<sup>26</sup>. This suggests that e/sQTL  
142 discovery power is a driving factor in tissue identity of the colocalizing e/sQTLs. We therefore  
143 primarily considered the causal genes proposed by the colocalization analysis and not the  
144 associated tissues, in downstream analyses.

145 We found that 58% of all GWAS loci tested significantly colocalized with at least one eQTL  
146 and/or sQTL based on eCAVIAR and/or *enloc*: 60% (76) of 127 cross-ancestry POAG GWAS loci,  
147 53% (36) of 68 European POAG loci and 59% (79) of 133 IOP loci (Fig. 2c and Supplementary  
148 Table 14). About 55% and 29% of GWAS loci colocalized with  $\geq 1$  eQTL and  $\geq 1$  sQTL, respectively.  
149 For 21% of the POAG and IOP GWAS loci (69 loci total), significant colocalization was found for  
150 the same e/sGene with eCAVIAR and *enloc* ('high confidence set' listed in Table 1 and  
151 Supplementary Table 15). The GWAS-e/sQTL colocalization analysis significantly reduced the  
152 number of putative causal genes per GWAS locus for POAG and IOP from an average of  $22.8 \pm$   
153 1.8 genes tested per LD interval (range: 3-166, median=15) to an average of  $3.5 \pm 0.4$  genes per  
154 locus (range: 1-36, median of 1 or 2 genes per locus per trait; Fig. 2d,e and Supplementary Table  
155 16). eQTLs and sQTLs nominated an average of 3 and 2 causal genes per locus, respectively, with  
156 partial overlap of target genes between the colocalizing eQTLs and sQTLs (Fig. 2e and  
157 Supplementary Table 16). 60-72% of the colocalizing e/sGenes per trait were protein-coding and  
158 18-20% were noncoding RNA genes, half of which were lincRNAs and half antisense genes (Fig.  
159 2f, Supplementary Tables 17-18, and Supplementary Note). A single causal gene was proposed  
160 for 80 (42%) of the POAG and IOP loci with significantly colocalizing e/sQTLs (Supplementary  
161 Tables 19-20), 49 (61%) of which are the nearest gene to the lead GWAS variant. In 30.3% (23/76),  
162 16.7% (6/36) and 31.7% (25/79) of the POAG cross-ancestry, POAG EUR and IOP GWAS loci,  
163 respectively, with significant colocalization results, the colocalizing e/sGenes were not the nearest  
164 gene to the lead GWAS variant. In total, 228, 118, and 279 genes, including previously suggested  
165 and novel ones, are candidate causal genes for POAG cross-ancestry risk, POAG EUR risk, and  
166 IOP variation, respectively (Supplementary Table 21), with a total of 459 genes proposed from the  
167 combined datasets.

168  
169 **Colocalizing e/sGenes of top POAG and IOP GWAS loci and direction of regulatory effect**  
170 **on disease risk.** In addition to prioritizing causal genes and regulatory mechanisms that may

171 contribute to POAG and IOP, colocalizing e/sQTLs propose the direction of effect of altered gene  
172 expression or splicing on disease risk or trait variation (examples for top POAG and IOP GWAS  
173 signals in Fig. 3 and Supplementary Fig. 5). For example, an eQTL and sQTL acting on *TMCO1*  
174 and an eQTL acting on *TMCO1*'s antisense, *RP11-466F5.8*, in the opposite direction, colocalized  
175 with the second strongest association with POAG (rs2790053, odds ratio (OR)=1.35; CLPP=0.92-  
176 1) and the top IOP association (rs116089225, beta = -0.744; CLPP=0.87-1) (Fig. 4a-e and  
177 Supplementary Fig. 6). Decreased expression of *TMCO1* and increased expression of *RP11-*  
178 *466F5.8* are proposed to lead to increased IOP levels and increased POAG risk (Fig. 4,  
179 Supplementary Fig. 6, and Supplementary Table 13). Furthermore, an alternative splice donor site  
180 in exon 4, the first exon in the *TMCO1* mRNA in GTEx Cells Cultured fibroblasts, leads to a longer  
181 exon 4 (Fig. 4f,g) that is associated with decreased POAG risk (Supplementary Tables 7 and 13).  
182 *TMCO1* is expressed in different cell types in the anterior and posterior parts of the eye, including  
183 lymphatic and fibroblast cells in the conventional and unconventional outflow pathways, vascular  
184 and immune cells in the anterior and posterior segments, and macroglial cells in the retina  
185 (Supplementary Figure 7). Other examples include *ANGPT1* and *ANGPT2*, involved in vascular  
186 biology, whose increased expression is proposed to reduce IOP levels (Supplementary Fig. 8 and  
187 Supplementary Table 13) that is consistent with the effect observed on IOP in *Angpt1*-knockout  
188 mice<sup>43</sup>.

189  
190 **Colocalizing genes for shared and distinct POAG and IOP loci.** Of 50 overlapping POAG and  
191 IOP GWAS loci, 39 (78%) of the loci had at least one significant colocalization result for both traits,  
192 and in all cases at least one common gene was implicated (Supplementary Table 13 and Table 1).  
193 In most of the cases (95%), the relative direction of effect of the colocalizing e/sQTLs on IOP was  
194 consistent with IOP's effect on POAG risk, proposing IOP-dependent mechanisms for POAG risk.  
195 For example, decreased *GAS7* expression or increased *ABO* expression were associated with both  
196 increased IOP levels and increased POAG risk (Supplementary Tables 7-13 and Supplementary  
197 Figs. 9-10). e/sGenes that colocalize with POAG loci not associated with IOP (48 loci; Column N  
198 in Supplementary Table 13) may suggest IOP-independent mechanisms.

199 To prioritize regulatory variants and genes that may affect POAG independent of IOP, we  
200 integrated retina Hi-C loops and/or epigenetically derived *cis*-regulatory elements (CREs) and  
201 super-enhancers (SEs) (Supplemental Data 4 in Marchal *et al.*<sup>40</sup>) with the POAG-only loci  
202 (Methods). In 17 of the loci,  $\geq 1$  colocalizing e/sQTLs was supported as a potential causal  
203 mechanism by retina Hi-C loops (6 loci), CREs (16 loci) and/or SEs (5 loci) (Supplementary Table  
204 22). This includes the strongest normal tension glaucoma (NTG) association (9p21)<sup>8,44</sup> in the POAG

205 cross-ancestry (rs944801 OR=1.26) and POAG EUR (rs6475604 OR=1.3) GWAS meta-analyses  
206 that colocalized with a *CDKN2A* eQTL in brain cortex, *CDKN2B-AS1* and *RP11-149I2.4* sQTLs in  
207 pituitary, and *CDKN2B* eQTL in skeletal muscle (Supplementary Table 13). The POAG risk variants  
208 and colocalizing e/sQTLs in this locus overlapped retinal CREs (Fig. 5a). These results imply that  
209 increased expression of *CDKN2A*, decreased expression of *CDKN2B*, and exon skipping in  
210 *CDKN2B-AS1* may increase POAG risk (Fig. 3, Supplementary Figs. 5a and 11). Other examples,  
211 involving a retina *SLC2A12* eQTL overlapping a retinal CRE, and e/sQTLs acting on *RERE* and its  
212 antisense, *RERE-AS1*, that are physically linked via retina chromatin loops to the *RERE*  
213 transcription start site (TSS), are shown in Fig. 5b and c (see also Supplementary Table 22).  
214 Notably, *RERE* expression is enriched in oligodendrocytes in the optic nerve head and optic nerve  
215 (False discovery rate (FDR)=0.07) and in retinal pigment epithelium (RPE) and S-cones in the  
216 macula (FDR=0.06), as shown below (Supplementary Table 38; Supplementary Fig. 18f, g).  
217

218 **Colocalizing genes in population-specific and cross-ancestry POAG loci.** For all 59 POAG  
219 EUR loci also found in the POAG cross-ancestry meta-analysis, at least one common colocalizing  
220 e/sGene was found for both the EUR and cross-ancestry GWAS (Supplementary Table 13). One  
221 such example is *EFEMP1*, in which rare mutations have been associated with a Mendelian form of  
222 glaucoma<sup>45</sup>. Colocalization analysis suggests that skipping of exons 6 and 7 in *EFEMP1* may be  
223 protective for POAG (Supplementary Fig. 12). Of the 9 loci found only in the POAG EUR GWAS,  
224 two loci colocalized with eQTLs acting on several genes each, including genes involved in the  
225 extracellular matrix (*EMID1*) and vascular endothelial growth (*ANGPTL2*), respectively, both of  
226 which also colocalized with IOP (Supplementary Table 23). In addition, three associations in the  
227 POAG cross-ancestry meta-analysis demonstrated significant allelic heterogeneity among the  
228 three populations (European, East Asian, and African American)<sup>8</sup>. e/sQTL colocalized with two of  
229 these loci. One is the 9p21 locus rs944801 with *CDKN2A/B* described above, which was significant  
230 in the European and Asian populations, but not the African population ( $P_{heterogeneity}=1.5 \times 10^{-8}$ )  
231 in which it is in lower frequency (AFR MAF=0.073, EUR MAF=0.42, EAS MAF=0.11 in gnomAD  
232 (URLs)). The other is a European-specific locus with the largest POAG odds ratio (rs74315329,  
233 OR=5.47). This variant is a nonsense mutation (p.Gln368Ter) in *MYOC*, known to cause juvenile-  
234 onset and adult-onset open-angle glaucoma with dominant inheritance<sup>46</sup>. This variant is 10-fold  
235 more common in the European population compared to the African population and is not found in  
236 the East Asian population (gnomAD; URLs). Of all the e/sQTL gene-tissue pairs that overlapped  
237 this locus targeting 24 genes, we identified an sQTL acting on *PIGC*, phosphatidylinositol glycan  
238 anchor biosynthesis class C, that significantly colocalized with the POAG cross-ancestry locus

239 (spleen CLPP=0.12, and arterial tissues RCP=0.26-0.34; Supplementary Table 13 and  
240 Supplementary Fig. 13). Conditioning on the nonsense variant in *MYOC* that is likely the primary  
241 causal variant in the locus, we found that a secondary haplotype colocalized with the *PIGC* sQTL  
242 (Supplementary Tables 24-28; more details in Supplementary Note). These results suggest that  
243 decreased exon 2 skipping in *PIGC* or increased *PIGC* expression may lead to increased POAG  
244 risk (Supplementary Fig. 13). *PIGC* is among 10 colocalizing POAG genes enriched in  
245 oligodendrocytes in the optic nerve head and optic nerve (See below; FDR=0.07, Supplementary  
246 Table 38; Supplementary Fig. 18f, g).

247  
248 **Mendelian randomization (MR) of colocalizing e/sQTLs.** To provide additional support for a  
249 causal relationship between e/sQTLs and POAG and/or IOP, we applied two-sample MR to all the  
250 significantly colocalizing e/sQTL and GWAS locus pairs based on eCAVIAR and/or *enloc*  
251 (Methods). We found evidence for a causal relationship (FDR < 0.05) for 348 (75%) genes that  
252 were robust to the influence of horizontal pleiotropy, where pleiotropy-robust sensitivity could be  
253 performed (Supplementary Table 29). A high-confidence list of putative POAG and/or IOP causal  
254 genes based on colocalization analysis and MR is provided in Table 1. We found 239 e/sGenes to  
255 have significant MR associations with both POAG and IOP, including *TMCO1*, *GAS7*, and *LMX1B*,  
256 which colocalized with the largest association signals for both POAG and IOP GWAS loci  
257 (Supplementary Figs. 5, 6, 9), and *DGKG* and *NPC2*, whose retina eQTLs colocalized with POAG  
258 and IOP. Sixty-eight genes had significant MR associations with IOP but not POAG, such as *HLA-*  
259 *B* and *SLC7A6*, and 41 genes had significant MR associations with POAG but not IOP, such as  
260 *CDKN2B-AS1*, *RERE*, and *YAP1*, proposing high-confidence IOP-independent mechanisms  
261 (Supplementary Table 29 and Fig. 5). Since the MR analysis could not be applied to the larger,  
262 better-powered POAG cross-ancestry GWAS, as it requires a similar population background  
263 between the e/sQTL and GWAS studies (European in our case), our downstream analyses were  
264 applied to the more inclusive list of proposed causal genes based on the colocalization analysis  
265 (Supplementary Table 13).

266  
267 **Enrichment of POAG and IOP colocalizing e/sGenes in biological processes.** To gain  
268 biological insight into ways the implicated genes might contribute to glaucoma pathogenesis, we  
269 next tested whether the target genes of all the colocalizing e/sQTLs with POAG cross-ancestry,  
270 POAG EUR, or IOP GWAS loci were enriched in specific biological pathways, gene ontologies, or  
271 mouse phenotype ontologies, using *GeneEnrich* (Methods and Fig. 1c). Genes that colocalized  
272 with POAG cross-ancestry loci were significantly enriched in elastic fiber formation (Empirical P-

273 value ( $P < 1 \times 10^{-5}$ , FDR < 0.001) and extracellular matrix organization ( $P = 3 \times 10^{-5}$ , FDR = 0.012), and  
274 nominally enriched ( $P < 0.05$ ) in the transforming growth factor beta (TGF) receptor signaling  
275 pathway ( $P = 3 \times 10^{-4}$ ) and abnormal eye morphology ( $P = 2.6 \times 10^{-3}$ ), amongst others (Supplementary  
276 Table 30 and Supplementary Fig. 14a,b). Genes that colocalized with POAG EUR loci were  
277 nominally enriched ( $P < 4 \times 10^{-3}$ ) in cellular senescence and cell cycle processes (e.g., Cyclin D-  
278 associated events in G1), lipid-related processes, such as apolipoprotein binding and decreased  
279 circulating high-density lipoprotein cholesterol level, and retina or neuronal related processes,  
280 including abnormal retina morphology, abnormal sensory neuron innervation pattern, and negative  
281 regulation of axon extension involved in axon guidance (Supplementary Table 31 and  
282 Supplementary Fig. 14c,d).

283 For the IOP genes, significant enrichment ( $P = 2 \times 10^{-5}$ , FDR = 0.025) was found in  
284 transcriptional regulation by *VENTX*, a gene that encodes a homeodomain-containing transcription  
285 factor (Supplementary Table 32 and Supplementary Fig. 14e). *VENTX* and its IOP-colocalizing  
286 target genes driving the gene set enrichment signal (*ANAPC1*, *ANAPC7*, *AGO4*, *MOV10*, *TCF7L2*)  
287 were most highly expressed in immune cell types, lymphocytes and macrophages, in the single cell  
288 anterior segment and optic nerve head described below (Supplementary Fig. 14f). The IOP genes  
289 were also significantly enriched (FDR < 0.15) in blood vessel morphogenesis and vasculature  
290 development, regulation of cytoskeletal organization, negative regulation of cellular component  
291 organization, and adherens junction (Supplementary Table 32 and Supplementary Fig. 14e). Since  
292 colocalization with multiple e/sQTLs was found for two GWAS loci in the HLA region on  
293 chromosome 6 associated with POAG and IOP (29 and 35 e/sGenes, respectively), likely due to  
294 high LD in the HLA region, we removed this region from the gene set enrichment analysis above  
295 to avoid inflating the results due to a single locus. When kept in, the endosomal vacuolar pathway,  
296 interferon gamma signaling, antigen presentation folding assembly and peptide loading of class I  
297 MHC, negative regulation of natural killer cell-mediated immunity, and cell aging were significantly  
298 enriched (FDR < 0.1) for POAG genes (Supplementary Table 33), in addition to the gene sets above.  
299 The colocalizing POAG and IOP genes driving the gene set enrichment signals are listed in  
300 Supplementary Tables 30-33.

301  
302 **Identifying pathogenic cell types for POAG and related ocular traits.** To further relate the  
303 implicated genes to pathogenic mechanisms and cell types, we next tested whether the expression  
304 of POAG or IOP colocalizing e/sGenes was enriched in specific cell types in key eye tissues  
305 implicated in the pathophysiology of POAG. We first applied ECLIPSER<sup>38,39</sup> (Methods and Fig. 1d)  
306 to 228, 118, and 279 e/sGenes that colocalized with POAG cross-ancestry, POAG EUR and IOP

307 GWAS loci, respectively (Supplementary Tables 13 and 34), and to cell type-specific expression  
308 from single nucleus (sn) RNA-seq of 13 tissues dissected from non-diseased human eyes: central  
309 cornea, corneoscleral wedge (CSW), trabecular meshwork (TM) including Schlemm's canal, iris,  
310 ciliary body (CB), lens<sup>36</sup> (all from anterior segment), peripheral and macular retina<sup>33,36</sup>, the optic  
311 nerve head (ONH), optic nerve (ON), peripapillary sclera (PPS), peripheral sclera, and choroid<sup>37</sup>  
312 (all from posterior segment) (Methods and Supplementary Tables 35-37). The cell type enrichment  
313 results are summarized in Supplementary Table 38.

314 In the anterior segment, we found significant enrichment (tissue-wide FDR<0.1) for POAG  
315 EUR loci in fibroblasts derived from the ciliary muscle (present in CB, CSW and TM<sup>36</sup>), annotated  
316 as ciliary fibroblasts in van Zyl *et al.*<sup>36</sup>, followed by fibroblasts derived from the iris root (present  
317 within the iris<sup>36</sup>), annotated as iris fibroblasts (Supplementary Table 38 and Fig. 6a,b). The ciliary  
318 muscle and iris are key tissues involved in the unconventional outflow pathway. These fibroblasts  
319 were also detected histologically within the TM where all three tissues meet and interweave at the  
320 iridocorneal angle<sup>36</sup>, implicating the conventional aqueous outflow pathway as well. Fig. 6c shows  
321 the e/sGenes driving the POAG EUR enrichment signal in ciliary fibroblasts. The POAG EUR genes  
322 were also modestly enriched in fibroblasts derived predominantly from the TM tissue (annotated as  
323 TM fibroblasts<sup>36</sup>) (P=0.014, FDR=0.18). For POAG cross-ancestry and IOP loci, we found  
324 supportive enrichment (P<0.05, FDR<0.23) in outflow pathway and cornea fibroblasts, vascular  
325 endothelium cells (cluster 2 derived from TM, CSW and CB tissues<sup>36</sup>), and lens epithelium, as  
326 detailed in Fig. 6a,d,e and Supplementary Table 38. Genes that colocalized with IOP loci were also  
327 significantly enriched (FDR<0.1) in pericytes (cluster 2 that localizes to the CSW<sup>36</sup>), and nominally  
328 enriched in lymphatic endothelium and Schlemm's canal, whose dysfunction can lead to elevated  
329 IOP<sup>47</sup> (Fig. 6e and Supplementary Table 38).

330 Clustering of the top-ranked anterior segment cell types (P<0.05) for POAG and IOP,  
331 separately, based on the overlap of genes driving the cell type enrichment, suggests three cell  
332 classes affecting POAG - fibroblasts, vascular endothelium, and lens epithelium; and three cell  
333 classes for IOP - fibroblasts, pericytes, and lymphatic endothelial cells (Fig. 6f, g). Between 45-  
334 78% of the genes driving the POAG enrichment signals in the outflow fibroblast cell types are  
335 common between the different fibroblasts (Fig. 6f), suggesting both shared and distinct genes  
336 acting in the conventional and unconventional outflow pathways. The IOP genes driving the  
337 enrichment signal in pericytes (Fig. 6h,i) were largely distinct from those enriched in vascular and  
338 fibroblast cell types (overlap 7-33%; Fig. 6g), and were enriched in vasculature development  
339 (P=3x10<sup>-5</sup>, FDR=0.075; Supplementary Table 40). On the other hand, the IOP genes driving the  
340 enrichment in TM fibroblasts (Supplementary Fig. 15c,d) were highly shared with the IOP genes

341 enriched in ciliary and iris fibroblasts (overlap 64-88%; Fig. 6g). Notably, the enrichment of IOP  
342 genes in pericytes was specific to IOP (asterisks in Fig. 6h). When ECLIPSER was applied to genes  
343 that colocalized with IOP loci not associated with POAG, only the enrichment in pericytes remained  
344 ( $P=0.007$ ) (Supplementary Table 41 and Supplementary Fig. 15e). Genes mapped to shared IOP  
345 and POAG loci were significantly enriched in ciliary and TM fibroblasts ( $FDR<0.01$ ) and lymphatic  
346 or vascular endothelial cells ( $FDR=0.026$ ). No enrichment was found for POAG-only loci in the  
347 anterior segment cell types, supporting IOP-dependent mechanisms in the anterior segment for  
348 POAG risk, as expected (Supplementary Table 41).

349 We next tested for enrichment of POAG and IOP colocalizing e/sGenes in retina snRNA-  
350 seq data (Methods). We found significant enrichment of POAG cross-ancestry genes in astrocytes  
351 and Müller glia cells ( $FDR<0.04$ ; Supplementary Table 38, Fig. 7a and Supplementary Fig. 16a),  
352 which replicated ( $FDR<0.06$ ) in a separate snRNA-seq study of the macula (Methods;  
353 Supplementary Table 38 and Supplementary Fig. 16g). Consistent results were found for POAG  
354 EUR genes (Supplementary Fig. 16b). A quarter (*YAP1*, *LPP*, *TRIB2*) of the 12 POAG cross-  
355 ancestry genes driving the astrocyte enrichment were common with Müller glia cells  
356 (Supplementary Fig. 16d, e), suggesting both shared and distinct processes between the two cell  
357 types. IOP genes were only nominally enriched in astrocytes ( $P=0.032$ ; Supplementary Fig. 16c).  
358 By testing POAG- or IOP-only loci and shared loci, the POAG enrichment in retinal astrocytes and  
359 Müller glia cells appears to be independent of IOP (Supplementary Table 41 and Supplementary  
360 Fig. 17; more details in Supplementary Note). The POAG cross-ancestry genes were also enriched  
361 in RPE cells and S-cones in the macula ( $FDR=0.06$ ). Of note, no significant enrichment was  
362 observed in RGCs (Fig. 7a), though some POAG colocalizing e/sGenes are expressed in RGCs  
363 (Supplementary Fig. 20).

364 Finally, we tested for cell type-specific enrichment in the optic nerve head (ONH), optic  
365 nerve (ON) and adjacent posterior tissues (Methods; Supplementary Table 37). The strongest  
366 enrichment ( $FDR<0.01$ ) of POAG cross-ancestry genes was found in fibroblasts primarily in the  
367 peripapillary sclera (PPS) that encompasses the ONH, followed by fibroblasts most abundant in  
368 the choroid, astrocytes that reside in the ONH and ON, Schwann cells in the choroid and PPS,  
369 oligodendrocyte precursor cells (OPCs) and oligodendrocytes in the ON and ONH (Supplementary  
370 Fig. 18f,g), and vascular endothelium cells primarily in the choroid ( $FDR<0.09$ ; Fig. 7b,c,  
371 Supplementary Table 38 and Supplementary Fig. 18a,d). POAG EUR genes showed similar  
372 enrichment patterns (Fig. 7b, Supplementary Fig. 18b and Supplementary Table 38). About half  
373 the genes driving the enrichment in astrocytes in ONH (Fig. 7d, e) and retina samples from separate  
374 donors were common (e.g., *DGKG*, *PLCE1*, *LPP*, *GAS7*, *YAP1*, and *COL11A1*; Supplementary

375 Table 38). *DGKG*, diacylglycerol kinase gamma, whose retina-specific eQTL colocalized  
376 (CLPP=0.96) with POAG cross-ancestry association (Fig. 7f) displayed the strongest cell type  
377 specificity in ONH (Fig. 7d) and retinal astrocytes (Supplementary Fig. 16d).

378 IOP genes were most significantly enriched in vascular endothelial cells and fibroblasts  
379 primarily residing in the choroid, but also in the ONH and PPS (FDR<0.014), followed by Schwann  
380 cells in the choroid and PPS, vascular smooth muscle cells (19-ACTA2; Supplementary Fig. 18h,i)  
381 in the PPS and sclera, pericytes (26-ACTA2) in the ONH, PPS and choroid, and OPCs in the ON  
382 (FDR<0.06; Fig. 7b, Supplementary Table 38, and Supplementary Fig. 18a,c,e). The IOP genes  
383 driving enrichment in vascular endothelial cells in the ONH, choroid and posterior tissues were  
384 enriched in vasculature development and anchoring junction gene ontologies (FDR<0.06), and IOP  
385 genes enriched in pericytes in the ONH, choroid and PPS were enriched in TIE2 signaling  
386 (FDR=0.02), response to carbohydrate adhesion (FDR=0.13), and negative regulation of cell  
387 adhesion (FDR=0.13) (Supplementary Table 40). Notably, the enrichment in oligodendrocytes and  
388 OPCs was specific to POAG-only loci, and enrichment in vascular endothelium and mural cells was  
389 specific to IOP-only loci (Supplementary Table 41 and Supplementary Fig. 19).

390 The cell type expression profiles of all POAG cross-ancestry, POAG EUR and IOP  
391 colocalizing e/sGenes is shown in Supplementary Fig. 20, and a summary of the cell types and  
392 pathways in which each of the POAG and IOP colocalizing e/sGenes are enriched is presented in  
393 Supplementary Tables 42-44. Applying ECLIPSER to various negative control traits suggests that  
394 the cell type enrichment results are specific to glaucoma and not due to unaccounted confounding  
395 factors (Supplementary Tables 45-46, Fig. 6a, and Supplementary Fig. 21; Supplementary Note).  
396 Furthermore, the ECLIPSER cell type enrichment significance did not correlate with cell count per  
397 cell type in the single-nucleus datasets (Pearson's  $R^2<0.2$ ,  $P>0.12$ ; Supplementary Table 47).

398 To increase confidence in the POAG and IOP cell type enrichment results, we applied two  
399 additional methods that identify cell types associated with complex traits, through regression  
400 analysis of genome-wide associations beyond known GWAS loci: stratified LD score regression  
401 (S-LDSC) and MAGMA (Fig. 1e; Methods). The primary enriched cell types for POAG and IOP  
402 found with ECLIPSER, including ciliary and TM fibroblasts, ONH fibroblasts, and retinal macroglial  
403 cells, were significant with S-LDSC (Supplementary Table 48; Supplementary Fig. 22) and more  
404 restrictively with MAGMA (Supplementary Table 49; Supplementary Fig. 22); additional enrichment  
405 was found in vascular types. Enrichment of POAG loci in ONH and ON oligodendrocytes was only  
406 found with ECLIPSER suggesting that the enrichment is primarily driven by genes with strong  
407 genetic effects. The cell type enrichment significance of ECLIPSER was reasonably correlated with  
408 that of S-LDSC and MAGMA (Average Pearson's  $r=0.53$ , range: 0.18-0.86; Supplementary Table

409 50). We further used conditional analysis implemented in MAGMA to test whether the different cell  
410 type enrichment signals for POAG or IOP were independent of each other in each tissue  
411 (Supplementary Table 51). In the anterior segment, the enrichment of POAG associations in ciliary  
412 fibroblasts was independent of TM fibroblasts, but not vice versa (Conditional P=0.04). In retina,  
413 POAG associations were significantly enriched in astrocytes ( $P<6E-8$ ) and Müller glia cells  
414 ( $P<0.002$ ), but only astrocytes remained significant after conditional analysis (Conditional  $P<4E-6$ ),  
415 suggesting that astrocytes may play a more important role in glaucoma pathogenicity than Müller  
416 Glia cells. In the ONH, the POAG and IOP enrichment in fibroblasts, astrocytes, vascular  
417 endothelium, and mural cells were all independent of each other (Supplementary Table 51).

418 Finally, to augment the POAG and IOP enrichment analysis, we tested for cell type  
419 enrichment of genes mapped to GWAS loci of additional glaucoma associated traits (listed in  
420 Supplementary Table 34), including vertical-cup-to-disc ratio (VCDR), cornea hysteresis, and  
421 central cornea thickness (Methods) in all ocular tissue regions (Supplementary Table 38, Fig. 6a  
422 and Fig. 7a, b). In the anterior segment, genes mapped to central corneal thickness and corneal  
423 hysteresis were most significantly enriched in corneal fibroblasts ( $FDR<0.007$ ; Fig. 6a and  
424 Supplementary Fig. 23a, b), highlighting the specificity of the POAG and IOP gene enrichment in  
425 the outflow pathway fibroblasts. The VCDR GWAS loci from a well-powered GWAS that used deep  
426 learning (ML) to score the characteristics of fundus images from 65,680 European individuals<sup>12</sup>  
427 showed significant enrichment in the TM fibroblasts from the conventional outflow pathway  
428 ( $FDR=0.02$ ; Fig. 6a and Supplementary Fig. 23c). TM fibroblasts were also the top nominally  
429 enriched cell type for a smaller VCDR GWAS, where 23,899 fundus images were manually scored  
430 by ophthalmologists<sup>13</sup> ( $P=0.0076$ ,  $FDR=0.3$ ; Fig. 6a and Supplementary Fig. 23d). In the retina, the  
431 ML-based VCDR loci displayed significant enrichment in GABAergic amacrine cells, cone  
432 photoreceptors and Müller glia cells ( $FDR<0.085$ ; Fig. 7a and Supplementary Fig. 23e) and nominal  
433 enrichment in astrocytes. In the ONH, the ML-based VCDR genes were nominally enriched in  
434 fibroblasts in the PPS, vascular endothelium primarily in the choroid, and astrocytes in the ONH  
435 and ON, similarly to POAG loci (Fig. 7b and Supplementary Fig. 23g, h; Supplementary Table 38).

436 In summary, our cell type enrichment analysis has revealed roles for both known and less  
437 well-studied cell types in POAG pathogenicity, such as fibroblasts in the unconventional and  
438 conventional outflow pathways, astrocytes in retina and ONH, OPCs in the ON and ONH, and  
439 Schwann cells and fibroblasts in the PPS and choroid. It also suggests known and new causal  
440 genes for POAG and related eye traits that may be affecting glaucoma susceptibility through  
441 specific cell types in the anterior and posterior parts of the eye in IOP-dependent and independent  
442 manners (Supplementary Tables 38 and 41).

443 **Discussion**

444

445 We report results of a systematic investigation of the underlying causal mechanisms, genes  
446 and cell types of over 130 cross-ancestry or European loci associated with POAG<sup>8,9</sup> and over 110  
447 loci associated with its major risk factor, elevated IOP<sup>9</sup>. Our analysis integrated a variety of  
448 datasets, including expression and splicing QTLs from 49 GTEx tissues<sup>26</sup> and from retina<sup>26,27</sup>,  
449 genome topology data from retina<sup>40</sup>, single-nucleus expression data from a whole-eye cell atlas  
450 that includes key structures of both the anterior<sup>36</sup> and posterior segments<sup>33,37</sup>, and the largest to  
451 date GWAS meta-analyses for these traits<sup>8,9</sup>. Our finding that eQTLs and sQTLs in GTEx tissues  
452 and retina are enriched for hundreds of known and more modest POAG and IOP associations,  
453 suggests a primary role for transcriptional regulation in POAG susceptibility, as observed for other  
454 diseases<sup>24-27</sup>, and implies that GTEx tissues can be used to uncover causal mechanisms for  
455 glaucoma. The GTEx e/sQTLs likely capture shared genetic regulation with the actual pathogenic  
456 tissues for glaucoma, such as fibroblasts and vascular endothelial cells, as well as shared  
457 regulation across cell types and tissues<sup>26</sup>.

458 Using two QTL/GWAS colocalization methods<sup>41,42</sup>, we prioritized putative causal genes for  
459 ~60% of the POAG and IOP GWAS loci. A similar fraction of GWAS loci with significant  
460 colocalization results has been found for other complex diseases and traits<sup>26,48</sup>. For a quarter (80)  
461 of the POAG and IOP loci, a single gene was proposed, ten of which are noncoding genes (lincRNA  
462 and antisense), suggesting that transcriptional and post-transcriptional gene regulation contribute  
463 to glaucoma susceptibility. We provided additional support for three quarters of the colocalizing  
464 e/sGenes using Mendelian randomization<sup>49,50,51</sup>, which tests for horizontal pleiotropy, not accounted  
465 for by Bayesian colocalization analysis<sup>52,53</sup>. For about one third of the GWAS loci, none of the  
466 proposed causal gene/s were the nearest gene to the lead GWAS variant, similar to that observed  
467 for other complex traits<sup>24,48,54</sup>. These results emphasize the value of using e/sQTLs or other  
468 functional assays that link regulatory regions to distal target genes<sup>24,55-57</sup> to prioritize causal genes  
469 underlying common variant associations.

470 Integrating e/sQTLs with POAG and IOP GWAS loci proposed both previously suggested<sup>8</sup>  
471 and new biological processes for these traits. The POAG colocalizing genes, which included  
472 several known mendelian, early-onset glaucoma genes (*EFEMP1*<sup>45,58</sup> and *LTBP2*<sup>59</sup>), were most  
473 strongly enriched in extracellular matrix organization and elastic fiber formation, as previously  
474 reported<sup>8</sup>, followed by TGF receptor signaling pathway. Structural changes of the extracellular  
475 matrix induced by TGF-beta2 in both the trabecular meshwork in the outflow pathway and the optic  
476 nerve head have been associated with POAG<sup>60</sup>, and have been suggested to cause impairment of

477 optic nerve axonal transport and neurotrophic supply that could influence RGC degeneration<sup>60</sup>.  
478 Regulation by the homeodomain transcription factor, VENTX, was the most significantly enriched  
479 gene set for IOP genes, which has not yet been associated with glaucoma. VENTX is proposed to  
480 play important roles during embryonic patterning (by homology), including in neural crest  
481 development<sup>61</sup>, as well as hematopoiesis, leukemogenesis, cellular senescence and macrophage  
482 differentiation<sup>62</sup>. Its strongest expression in our single cell data was in lymphocytes in the anterior  
483 segment, and macrophages in the optic nerve head, proposing a novel link between immune-  
484 related processes and IOP levels. Reduced circulating endothelial progenitor cells has been  
485 reported in POAG patients<sup>63</sup>, which could explain impaired flow-mediated vasodilation in POAG<sup>64</sup>.  
486 Additional processes suggested to affect IOP regulation, aside from previously suggested<sup>9</sup> vascular  
487 development, are regulation of cytoskeleton organization, and adherens junction, a cell-cell junction  
488 whose cytoplasmic face is linked to the actin cytoskeleton, and that allows cells to respond to  
489 biomechanical forces and structural changes in the tissue microenvironment<sup>65</sup>. Inhibition of  
490 adherens junction regulation in trabecular meshwork has been shown to modestly influence IOP  
491 levels in rabbits<sup>66</sup>. We also found modest enrichment of POAG genes in neuronal-related  
492 processes, including genes affecting retinal morphology, sensory neuron innervation pattern, and  
493 regulation of axon guidance. These genes may represent IOP-independent mechanisms, which  
494 will need to be corroborated in future GWAS with larger numbers of normal tension glaucoma  
495 cases.

496 In addition to prioritizing causal genes for POAG and IOP, e/sQTLs suggest the direction of  
497 effect of gene expression changes or alternative splicing on disease risk that could inform drug  
498 design. In this study, we provide various hypotheses of putative causal genes and regulatory  
499 mechanisms that may affect POAG susceptibility in an IOP-dependent or independent manner, for  
500 experimental follow up. For example, an increase in expression or alternative splicing of *TMCO1*,  
501 a gene that regulates the balance of calcium ions inside the endoplasmic reticulum, or a decrease  
502 in expression of *LMX1B*, LIM homeobox transcription factor 1 beta, that is essential for several  
503 developmental processes including the anterior segment of the eye<sup>67</sup>, were proposed to reduce  
504 POAG risk and IOP levels. The lead IOP GWAS variant (rs116089225) in *TMCO1* that colocalized  
505 with *TMCO1* e/sQTLs has been recently associated with variable number tandem repeat (VNTR)  
506 length in the UK biobank study<sup>68</sup>. However, the VNTR did not display allelic series association with  
507 *TMCO1* expression levels in GTEx<sup>68</sup>, suggesting that the GWAS variant might be tagging more  
508 than one causal mechanism. As for IOP-independent mechanisms, an sQTL acting on *CDKN2B-*  
509 *AS1*, which leads to skipping of exons 2 and 3 that overlap the *CDKN2B* gene on the opposite  
510 strand, is proposed as a potential mechanism of action for the protective signal found in this gene<sup>69</sup>.

511 Skipping of these exons might render the *CDKN2B* antisense less efficient in forming a complex  
512 with the *CDKN2B* RNA. Retinal Hi-C and epigenetic data further support potential roles for e/sQTL  
513 effects on POAG in the retina, such as increased expression of *RERE* (arginine-glutamic acid  
514 dipeptide repeats) proposed to increase POAG risk. Of note, *RERE* has also been associated with  
515 VCDR<sup>13</sup>. Overexpression of the *RERE* protein that co-localizes with a nuclear transcription factor  
516 triggers apoptosis, and its deficiency in mice causes retinal and optic nerve atrophy<sup>70</sup>. This study  
517 also suggested a potential secondary causal gene, *P/GC* for the strongest POAG association, a  
518 nonsense mutation in *MYOC*, which will need to be replicated in a larger independent POAG  
519 GWAS. The *MYOC* mutation causes aggregation of misfolded myocilin proteins in the trabecular  
520 meshwork, which may lead to elevated IOP levels<sup>71</sup>. Conversely, the enrichment of *P/GC* (that  
521 encodes an endoplasmic reticulum-associated protein) expression, along with other POAG-  
522 colocalizing genes, in oligodendrocytes in the optic nerve head (ONH), suggests a secondary  
523 causal role for this locus in RGC support, in the posterior part of the eye.

524 There are several reasons why we may not have found colocalizing e/sQTLs for 40% of the  
525 loci. First, some of the causal genes or regulatory effects may be specific to regions in the eye or  
526 rare cell types for which we do not yet have representative e/sQTLs. Second, some genes may  
527 affect POAG or IOP by perturbing processes only active during development or under specific  
528 conditions or stimuli, not captured in adult tissues. Third, the causal variant may be another type of  
529 molecular QTL not tested in this study, such as e/sQTL acting in *trans* or protein QTLs. Fourth,  
530 some of the genetic associations may be tagging deleterious protein-coding variants<sup>8</sup>. Finally, there  
531 are several limitations to Bayesian colocalization methodologies<sup>52,53</sup>, as described in the  
532 Supplementary Note.

533 By applying a novel method (ECLIPSER<sup>38,39</sup>) to the colocalizing e/sGenes and single  
534 nucleus expression data from glaucoma-relevant eye tissues, we provided support for previously  
535 implicated cell types affecting POAG development, and shed light on less well-established or novel  
536 pathogenic cell types for POAG and IOP. One of the unique features of ECLIPSER, compared to  
537 other single cell enrichment methods<sup>72-76</sup> is that it identifies cell types that are specific to a given  
538 disease or trait, compared to a range of unrelated complex diseases and traits. Our results found  
539 that gene expression variation in the ciliary and iris fibroblasts in the unconventional outflow  
540 pathway in the anterior segment, in addition to the TM cells and Schlemm's canal cells in the  
541 conventional outflow pathway, may both be key contributors to local IOP regulation and POAG risk.  
542 The expression profile of the ciliary fibroblasts that was most strongly enriched for POAG genes, is  
543 most similar to the 'beam cell A' defined in the single cell RNA-seq atlas of the outflow pathway in  
544 van Zyl *et al.*<sup>34</sup> (Fig. S6B in <sup>34</sup>), which populates the ciliary muscle and uveal base of the TM; the

545 iris fibroblasts are most similar to 'beam cell B', and the TM fibroblasts to the JCT (juxtacanalicular  
546 trabecular meshwork) cell type that resides adjacent to the Schlemm's canal. Since the role of the  
547 unconventional outflow pathway in IOP homeostasis remains relatively understudied compared to  
548 that of the conventional pathway<sup>77</sup>, these findings may encourage further avenues of investigation.  
549 Furthermore, the enrichment of IOP genes in pericytes, many of which are not currently associated  
550 with POAG, extends our understanding of how genetic variation may be affecting IOP in the anterior  
551 segment. Pericytes are mural cells that wrap around the endothelial cells that line capillary blood  
552 vessels. A recent study has found reduced capillary diameter and impaired blood flow at pericyte  
553 locations in mouse eyes with high IOP<sup>78</sup>.

554 In the peripheral and macular retina, we found significant enrichment of POAG colocalizing  
555 genes in astrocyte and Müller glia cells. Astrocyte and Müller glia are two types of macroglia cells  
556 that interact with RGCs and blood vessels, and play an important role in retinal homeostasis,  
557 including metabolic supply and structural support, maintaining the extracellular environment of the  
558 neurons, and neurotransmitter transmission. Müller glia, the most common glial cell in the retina,  
559 span the entire retinal layer, while astrocytes are present only in the innermost layer of the retina.  
560 Several studies in animal models and patients with glaucoma<sup>79-81</sup> have found that astrocytes and  
561 Müller glia cells become reactive at early stages of glaucomatous conditions when RGCs are intact,  
562 suggesting a role for macroglia in the initiation and progression of glaucoma. POAG genes, but not  
563 IOP genes, were also enriched in astrocyte types residing primarily in the ONH that contains the  
564 lamina cribrosa (LC)<sup>82</sup>, a mesh-like structure where unmyelinated RGCs pass through the sclera to  
565 exit the eye, and another in the ONH and optic nerve (ON). Notably, astrocytes have been found  
566 to be one of the major cell types isolated from human ONH<sup>82</sup> and in LC dissected from human  
567 ONH<sup>83</sup>, and make up ~20% of the cells in our ONH snRNA-seq dataset.

568 In the ONH and surrounding posterior tissues, POAG genes were most strongly enriched  
569 in fibroblasts abundant in the peripapillary sclera (PPS), which surrounds the ONH. Pressure on  
570 the ONH and PPS that is a continuum of the LC can cause astrocyte reactivity and compression of  
571 RGC axons that can lead to RGC death<sup>84,85</sup>. Genes mapped to POAG, but not IOP loci were also  
572 enriched in oligodendrocytes that form a myelin sheath around the axons of RGCs, and  
573 oligodendrocyte precursor cells found in the ON, suggesting new IOP-independent mechanisms  
574 that can affect optic nerve degeneration. The strongest enrichment for IOP was in vascular  
575 endothelial (also enriched for POAG genes) and fibroblast cells primarily residing in the choroid,  
576 but also in the ONH and PPS, suggesting that vascular structural abnormalities or functional  
577 dysregulation of blood flow to the optic nerve and retina may be an important contributor to POAG<sup>86</sup>.  
578 It is also possible that the enrichment in the ONH vascular endothelial cells is capturing causal

579 mechanisms acting in the vascular endothelial cells in the anterior segment that were enriched for  
580 most of the same IOP genes as in ONH. The IOP genes were also enriched in vascular smooth  
581 muscle cells (VSMC) in the PPS and sclera. These VSMC-specific genes were enriched in lipid  
582 binding and negative regulation of cell substrate adhesion processes, suggesting a role in  
583 cytoskeleton-associated cell-cell adhesion and cell-extracellular matrix adhesion. These muscle  
584 cells may be part of the LC, as LC cells isolated from human ONH were found to stain for alpha-  
585 smooth muscle actin<sup>82,83</sup>. Cells in the LC produce extracellular matrix proteins to support the LC  
586 structure<sup>83</sup>, and biomechanical strain on the LC, such as from elevated IOP, is thought to be one  
587 of the causes of RGC degeneration<sup>87,88</sup>. Further investigation will be needed to determine whether  
588 the muscle cells found in the ONH single nucleus dataset<sup>37</sup> reside in the LC or in other structures  
589 such as blood vessels.

590 Notably, we did not find significant enrichment of cell type-specific expression of POAG or  
591 IOP genes in RGCs, whose cell death is the key characteristic of glaucoma, but rather in neuronal  
592 support cells. This highlights the importance of targeting the support cells in new therapy design. It  
593 should be noted that multiple colocalizing POAG genes are expressed in RGCs (see  
594 Supplementary Fig. 20 and Monavarfeshani *et al.*<sup>37</sup>), however they are also expressed in other  
595 retinal cell types. Hence, the potential effect of these genes on POAG via RGCs merits further  
596 investigation. Furthermore, while several studies have suggested that microglia, specialized  
597 macrophage-like cells, may affect RGC survival<sup>89</sup>, we did not find support for a causal role of  
598 microglia or immune cells in POAG susceptibility. A less expected result was the enrichment of  
599 POAG genes in RPE cells, which was also shown in the posterior ocular cell atlas<sup>37</sup>. In all, our  
600 findings in retina, ONH and the surrounding tissues propose cell types and biological processes  
601 that may be viable targets for neuroprotective therapies.

602 A potential limitation of our GWAS-cell type enrichment method, ECLIPSER is that it only  
603 considers genes that map to genome-wide significant loci and not subthreshold associations. We  
604 thus provided further support for our cell type enrichment results using two additional methods,  
605 stratified LD score regression and MAGMA, that analyze multiple modest associations genome-  
606 wide in addition to known GWAS loci. Furthermore, ECLIPSER primarily considers genes whose  
607 expression is specific to one or few cell types within a tissue, as the cell type specificity scoring  
608 metric was found to be successful in identifying known pathogenic cell types for a range of complex  
609 diseases and traits in a cross-tissue single nucleus expression atlas using GTEx samples<sup>38</sup>. We  
610 note though that genes expressed at similar levels across most or all cell types may also contribute  
611 to disease risk or trait variation and would be missed with this approach.

612 In conclusion, our work has generated new insights into POAG mechanisms, which could  
613 inform the development of novel therapies targeting IOP reduction and neuroprotection. By  
614 integrating genetic regulation and single cell expression in glaucoma-relevant ocular tissues with  
615 GWAS summary statistics we have identified known and new causal genes and biological  
616 processes; proposed key ocular cell types that may be pathogenic for glaucoma; and provided  
617 evidence for the existence of hundreds of novel genetic associations of regulatory effects for  
618 glaucoma. In the future, detection of e/sQTLs in relevant eye tissues and at the cellular level<sup>90,91</sup> is  
619 expected to provide a more complete picture of the causal molecular and cellular mechanisms of  
620 POAG risk and IOP variation.

621

## 622 **Methods**

623

624 **GWAS datasets.** We applied colocalization and fine-mapping analysis to 127 GWAS loci identified  
625 in the cross-ancestry POAG GWAS meta-analysis of 34,179 cases and 349,321 controls from  
626 European, African, and East Asian populations<sup>8</sup>, 68 GWAS loci from the GWAS meta-analysis of  
627 the European subset of 16,677 POAG cases and 199,580 controls<sup>8</sup>, and 133 LD-independent  
628 GWAS variants in 112 loci from the IOP GWAS meta-analysis of 139,555 primarily UK Biobank  
629 (European) samples<sup>9</sup>. The GWAS meta-analysis summary statistics, which included p-value, effect  
630 size and standard error, were obtained from the corresponding studies. Chromosome positions  
631 were lifted over from genome build 37 (hg19) to hg38. Association results on chromosome X were  
632 only available for the POAG GWAS meta-analyses (cross-ancestry and European subset).

633

634 **GTEx and EyeGEx QTL datasets.** *cis*-eQTLs and *cis*-sQTLs from 49 tissues from GTEx release  
635 v8<sup>26</sup> and *cis*-eQTLs from peripheral retina<sup>27</sup> were used in this study. Summary statistics of all  
636 variant-gene e/sQTL pairs tested in each of the 50 tissues, the significant e/sGenes and e/sVariants  
637 at FDR<0.05, and the gene expression levels and LeafCutter<sup>92</sup> values are available for download  
638 from the GTEx portal (URLs). The summary statistics of all variant-gene pairs tested per gene and  
639 tissue was used as input to the colocalization analysis, and the LocusZoom<sup>93</sup> and LocusCompare  
640 plots (URLs). Plots of exon and exon junction read counts were taken from the visualizations on  
641 the GTEx portal (URLs). GENCODE versions 26 and 25 were used for the GTEx v8 and EyeGEx  
642 studies, respectively.

643

644 **Enrichment of POAG and IOP associations among e/sQTLs using QTLEnrich.** To test whether  
645 genome-wide significant and nominal POAG and IOP trait associations are enriched among eQTLs

646 and sQTLs, and to assess the contribution of e/sQTLs to these traits, we applied *QTLEnrich*<sup>24,26</sup> to  
647 the POAG and IOP GWAS meta-analyses summary statistics, using eQTLs and sQTLs from the  
648 49 GTEx tissues<sup>26,27</sup> and eQTLs from peripheral retina (EyeGEx<sup>27</sup>). *QTLEnrich* is a rank and  
649 permutation-based method that evaluates the fold-enrichment significance of trait associations  
650 among a set of e/sQTLs in a given tissue, correcting for three confounding factors: minor allele  
651 frequency (MAF), distance to the target gene's transcription start site, and local LD<sup>24</sup> (for more  
652 details see Supplementary Note). Only protein-coding and lincRNA genes were considered in this  
653 analysis. Significant tissues were determined based on an Enrichment P-value that passed  
654 Bonferroni correction, correcting for 50 tissues and two QTL types tested ( $P < 5 \times 10^{-4}$ ). The adjusted  
655 fold-enrichment was used to rank the significantly enriched tissues, as this statistic is not correlated  
656 with tissue sample size or number of significant e/sQTLs per tissue<sup>24</sup>, as observed with the  
657 colocalization analysis (Supplementary Fig. 4). For the significant trait-tissue pairs, the fraction and  
658 number of e/sVariants proposed to be associated with POAG or IOP were estimated using an  
659 empirically derived, true positive rate (Adj.  $\pi_1$ ) approach that we implemented in the latest version  
660 of *QTLEnrich* (URLs), based on Storey's analytical  $\pi_1$ <sup>94,95</sup> and an empirical FDR method<sup>94,95</sup> (see  
661 Supplementary Note).

662  
663 **Colocalization analysis.** To identify a high confidence set of genes and regulatory mechanisms  
664 (e/sQTLs) that may be mediating the functional mechanisms underlying known common variant  
665 associations with POAG and IOP, we applied two Bayesian-based colocalization methods:  
666 eCAVIAR<sup>41</sup> and *enloc*<sup>42</sup>. These methods assess the probability that co-occurring GWAS and  
667 e/sQTL signals are tagging the same causal variant or haplotype, accounting for local LD and allelic  
668 heterogeneity, using slightly different fine-mapping and colocalization approaches. They are  
669 applied to GWAS and QTL summary-level statistics enabling the analysis of large, well-powered  
670 GWAS meta-analyses, for which genotype data are not available. For the *enloc* analysis, DAP-G<sup>42</sup>  
671 was used to perform fine-mapping of GWAS and e/sQTL loci to estimate the posterior probabilities  
672 of each variant in each locus being the causal variant, while eCAVIAR has the fine-mapping feature  
673 built in. We applied the two colocalization methods to 127 POAG cross-ancestry GWAS, 68 POAG  
674 GWAS loci from the European subset meta-analysis, and 133 independent IOP variants (112 loci)  
675 from a primarily European study (described above). Z-scores from the GWAS and GTEx e/sQTL  
676 studies, computed as the effect size (beta) divided by the standard error of the effect size for each  
677 variant, were used as input into eCAVIAR and DAP-G. For the retina eQTLs, we computed z-scores  
678 from the variant association p-values assuming a chi-square distribution with 1 degree of freedom.

679 All GWAS loci were tested for colocalization with all eQTLs and sQTLs from 49 GTEx  
680 tissues<sup>26</sup> and peripheral retina eQTLs<sup>27</sup> that had at least 5 e/sVariants (FDR<0.05) within the GWAS  
681 locus LD interval. An LD window around each lead GWAS variant was defined as the chromosome  
682 positions on either side containing variants within  $r^2 > 0.1$ , determined using 1000 Genomes Project  
683 Phase 3<sup>96</sup> as the reference panel, and extending an additional 50kb on either side. For the IOP and  
684 POAG EUR loci, LD was computed using only the European samples in 1000 Genomes Project,  
685 while for the cross-ancestry POAG loci, LD was computed using the European, African, and East  
686 Asian samples in 1000 Genomes. If a GWAS variant was not found in 1000 Genomes, an LD proxy  
687 variant ( $r^2 > 0.8$ ) was searched for in GTEx, and if not found, the nearest variant was used. The  
688 interval boundaries and number of variants tested are reported in Supplementary Tables 7-13.  
689 eCAVIAR and *en/loc* analyses were applied to all common variants (MAF>1%) that fell within the  
690 GWAS LD intervals and were present in both the GWAS and e/sQTL studies. The effect allele of  
691 the variants in each GWAS was aligned relative to the alternative (ALT) allele that was used as the  
692 effect allele in GTEx and EyeGEx. Colocalization analysis of the retina eQTLs was only performed  
693 using eCAVIAR. GWAS-e/sQTL-tissue combinations with a colocalization posterior probability  
694 (CLPP) above 0.01 were considered significant with eCAVIAR and/or with an RCP above 0.1 were  
695 considered significant with *en/loc* based on the methods' recommendations<sup>41,42,52</sup>. To remove  
696 potential false positives, we filtered out variant, gene, tissue, trait combinations where the  
697 e/sVariant with a significant colocalization result had a GWAS p-value above  $1 \times 10^{-5}$  or whose  
698 e/sQTL p-values was above  $1 \times 10^{-4}$  and/or did not pass FDR<0.05 (FALSE in column  
699 'Pass\_QC\_QTL\_FDR05\_P1E04\_GWAS\_P1E05' in Supplementary Tables 7-12). Further details  
700 on the eCAVIAR and *en/loc* analyses and quality control can be found in Supplementary Note.

701 **Mendelian randomization (MR).** Mendelian randomization (MR)<sup>51</sup> was used to provide additional  
702 genetic support for a causal relationship between colocalizing e/sQTLs and POAG and/or IOP loci.  
703 Significant e/sVariants were used as the instrumental variable (IV) in MR to facilitate causal  
704 inference<sup>97</sup> (See Supplementary Note). Two sample MR was applied to the summary statistics of  
705 the e/sQTLs (exposure) and POAG or IOP GWAS (outcome) for all significant colocalizing loci  
706 (Supplementary Tables 7-12), using the *TwoSampleMR* and *MendelianRandomization* packages  
707 in R (version 4.1.2)<sup>98</sup>. To avoid confounding by ancestry, MR was conducted using the European  
708 ancestry subset of the POAG GWAS and the IOP GWAS, which primarily contains European  
709 individuals. MR estimates were generated by calculating the Wald ratio, i.e., the variant-outcome  
710 association beta divided by the variant-exposure association beta<sup>99</sup>. Where multiple variants  
711 constituted the instrument for the candidate gene, the inverse-variance weighted (IVW) method

712 was used as the primary method for pooling variant-specific estimates<sup>100</sup>. Given that the IVW  
713 approach assumes no horizontal pleiotropy, methods robust to violation of the exclusion-restriction  
714 assumption were used as sensitivity analyses. The simple-median<sup>101</sup>, weighted-median<sup>101</sup>, MR-  
715 Egger<sup>102</sup>, and MR-PRESSO<sup>103</sup> methods were applied. Horizontal pleiotropy was tested using the  
716 Egger-intercept test and the MR-PRESSO global heterogeneity test, for which  $P < 0.05$  indicated  
717 the presence of horizontal pleiotropy. MR associations with Benjamini-Hochberg (BH) FDR  $< 0.05$   
718 for the primary IVW/Wald ratio test were considered statistically significant. In cases where  
719 horizontal pleiotropy was found based only on the MR-PRESSO global heterogeneity test, an MR  
720 PRESSO outlier-corrected p-value  $< 0.05$  was considered a significant result.

721 **Integration of retina Hi-C and epigenetic data with colocalizing POAG loci and e/sQTLs.** To  
722 identify retina eQTLs or GTEx e/sQTLs that colocalized with POAG GWAS loci that may be exerting  
723 their causal effect on POAG in the retina, we inspected all POAG loci in the context of chromatin  
724 loops, *cis* regulatory elements (CREs) and super-enhancers (SEs) that were previously detected  
725 in retina from 5 postmortem non-diseased human donor eyes<sup>40</sup>. The loops were calculated from  
726 Hi-C (3D chromosome conformation capture) data, and the CREs and SEs from epigenetic data,  
727 as described in Marchal *et al.*<sup>40</sup>. The lead POAG GWAS variants and their LD proxy variants  
728 ( $r^2 > 0.8$ ), the colocalizing e/sQTLs and LD proxy variants, which are also significant e/sVariants  
729 (FDR  $< 0.05$ ), and the e/sQTL target genes were inspected for overlap or closest overlapping gene  
730 with the Hi-C loops, CREs, and SEs, using the closestBed command from bedtools (v2.27.1)<sup>104</sup>.  
731 For retina eQTLs and GTEx e/sQTLs GENCODE versions 25 and 26 were used, respectively, to  
732 overlap genes and TSS hg38 coordinates. Colocalizing e/sQTLs were proposed as putative causal  
733 genes to POAG, if the e/sVariant overlapped one foot of the loop and the second foot overlapped  
734 the gene body or TSS of the target gene. CRE and SE target genes were defined if the e/sVariant  
735 and gene body or TSS of the gene overlapped the same CRE or SE. The closest target genes  
736 identified using chromatin loops for the POAG cross-ancestry GWAS loci was taken from our  
737 recently published Hi-C study (Supplemental Data 4 in Marchal *et al.*<sup>40</sup>).  
738

739 **Single nucleus RNA-seq datasets and differential gene expression.** We analyzed gene  
740 expression values ( $\log(TPK+1)$ ) from four single-nucleus (sn) RNA-seq data sets from the following  
741 glaucoma-relevant regions of the eye: anterior segment<sup>36</sup>, retina<sup>33,36</sup>, macula<sup>36</sup>, and optic nerve  
742 head and surrounding posterior tissues<sup>37</sup>. All tissue samples were dissected from non-diseased  
743 eye globes from post-mortem donors with no record of eye disease, and were de-identified. The  
744 number of cells per cell types in each of the tissues can be found in Supplementary Table 38.

745 Differential gene expression was applied to genes expressed in at least 5% of cells in any cell type  
746 cluster in each of the datasets. Here is a brief description of the four datasets:

747 **Anterior segment:** Six tissues in the anterior segment, including central cornea,  
748 corneoscleral wedge (CSW), trabecular meshwork (TM), iris, ciliary body (CB) and lens, were  
749 dissected from six donors within 6 hours from death, as described in<sup>36</sup>. To be able to compare  
750 across cell types between tissues in the anterior segment, the snRNA-seq data from cornea, CSW,  
751 CB, iris, and TM were pooled, downsampled to 1000 cells per type in each tissue, and reclustered  
752 yielding 34 clusters<sup>36</sup>. Five clusters were identified for the lens. Differential gene expression  
753 analysis between each cell type and all other cell types was performed using the regression model  
754 in MAST<sup>105</sup> that corrects for the proportion of genes expressed per cell.

755 **Retina:** Retina samples from the fovea (4mm punch), macula (6 mm punch) and/or  
756 periphery were collected from six donors within 6 hours from death from the Utah Lions Eye Bank,  
757 flash frozen and processed as described in<sup>33</sup> (more details in Supplementary Note). The number  
758 of cells from the three retinal regions from each donor is given in Supplementary Table 35. snRNA-  
759 seq data from RGCs from a few additional donors were added to the data set, given the relevance  
760 of RGCs to glaucoma, though RGCs still only comprised about 1/250 of the total data set.  
761 Differential gene expression for each cell type in the ml\_class level used in this study was computed  
762 using the Wilcoxon rank sum test.

763 **Macula:** Macular samples were dissected with 8mm punches from five donors within 4  
764 hours of death at the University of Utah (Supplementary Table 36). For three of the samples, RGCs  
765 were enriched by staining the nuclei with NEUN antibody (Millipore Sigma, #FCMAB317PE)  
766 followed by FACS sorting. The macular samples were processed similarly to the optic nerve head  
767 samples below. Differential gene expression for each cell type compared to all other cell types was  
768 computed using the MAST method<sup>105</sup>.

769 **Optic nerve head and posterior tissues:** The optic nerve head, including peripapillary  
770 tissues, was dissected with 4 mm punches from 13 donors, the optic nerve was dissected from 7  
771 donors, peripapillary sclera from 4 donors, sclera from 3 donors, and choroid from 5 donors, within  
772 a median of 6 hours from death at either the University of Utah or Massachusetts General Hospital  
773 (Supplementary Table 37). Further description of the tissues' dissection, single-nuclei isolation, and  
774 snRNA-sequencing can be found in Supplementary Note and Monavarfeshani *et al.*<sup>37</sup>. snRNA-seq  
775 data processing and analyses were performed similarly to the pipeline used for the anterior  
776 segment in van Zyl *et al.*<sup>36</sup>. Thirty-six cell type clusters were identified across the five tissues.  
777 Differential gene expression (DGE) was computed using the MAST method<sup>105</sup>, comparing the cells  
778 from each cell type to all other cells, excluding cells from the same cell class similar to the cell type

779 of interest, aside for the given cell type (e.g., excluding all fibroblast cell types when computing  
780 DGE for cell type, 5-Fibro).

781

782 **Cell type-specific enrichment of genes that map to GWAS loci for a given complex trait using**  
783 **ECLIPSER.** To identify ocular cell types that are enriched for cell type-specific expression of genes  
784 mapped to GWAS loci of POAG, IOP and related traits, we extended a method we recently  
785 developed called ECLIPSER (Enrichment of Causal Loci and Identification of Pathogenic cells in  
786 Single Cell Expression and Regulation data)<sup>38,39</sup>, to target genes of colocalizing e/sQTLs.  
787 ECLIPSER assesses whether genes mapped to a set of GWAS loci for a given complex disease  
788 or trait are enriched for cell type-specific expression compared to the cell type specificity of genes  
789 mapped to a background (null) set of GWAS loci associated with hundreds of unrelated traits. The  
790 underlying assumption of ECLIPSER is that multiple (though not necessarily all) trait-associated  
791 genes will be more highly expressed in a given pathogenic cell type compared to non-pathogenic  
792 cell types in a tissue of action, more so than unrelated traits. The analysis consisted of the following  
793 main steps: **(i) Mapping genes to GWAS loci.** For the POAG and IOP traits, e/sQTL colocalization  
794 analysis was used to prioritize genes in GWAS loci. For the cornea-related, VCDR and negative  
795 control traits, genes were mapped to GWAS loci if they were target genes of a GTEx or retina  
796 e/sQTL that was in LD ( $r^2 > 0.8$ ) with the GWAS locus (since colocalization analysis for these traits  
797 was beyond the scope of this paper). The genome-wide significant variants associated with the  
798 cornea traits and negative control traits were taken from Open Targets Genetics<sup>106</sup>, and for  
799 physician and machine learning-based VCDR measures from the corresponding published GWAS  
800 meta-analyses<sup>12,13</sup>. **(ii) Null set of GWAS loci.** We compiled a null set of GWAS loci, by selecting  
801 all genome-wide significant associations for a range of complex traits in Open Targets Genetics<sup>106</sup>  
802 that were taken from the NHGRI-EBI GWAS catalog and UK Biobank GWAS studies. We excluded  
803 from the null set variants associated with any ocular trait. **(iii) LD clumping of loci.** We collapsed  
804 GWAS variants that were in LD with each other ( $r^2 > 0.8$ ) or that shared a mapped gene into a single  
805 locus for the set of GWAS loci for each ocular or negative control trait and for the null set,  
806 separately, to avoid inflating the cell type enrichment results due to LD<sup>39</sup>. **(iv) Cell type specificity**  
807 **locus score.** We scored each GWAS locus for the ocular traits and the null set as the fraction of  
808 genes mapped to the locus, that demonstrated cell type specificity (defined here as fold-change  $>$   
809 1.3 and FDR  $< 0.1$ ). Only genes expressed in at least 5% of cells in any cell type cluster were  
810 included in the analysis. **(v) Assessing cell type-specificity of GWAS locus set.** We estimated  
811 a cell type specificity fold-enrichment and p-value per trait (GWAS locus set), tissue and cell type  
812 combination, compared to the null GWAS locus set, using a Bayesian Fisher's exact test and the

813 95th percentile of the null locus scores for the cell type specificity cutoff. The Bayesian approach  
814 enables estimating 95% confidence intervals of the fold-enrichment, including for traits that have  
815 few or no loci that fall above the enrichment cutoff<sup>39</sup>. **(vi) Cell type specific disease-contributing**  
816 **genes.** Cell type-specific genes mapped to GWAS loci whose score was equal to or above the 95th  
817 percentile enrichment cutoff in significantly enriched cell types ('leading edge loci') were proposed  
818 to influence the given complex trait in the given cell type ('leading edge genes'), though it is possible  
819 that some of these genes are affecting the given trait through other cell types. Cell types with a  
820 tissue-wide Benjamini-Hochberg FDR equal to or below 0.1, correcting for the number of cell types  
821 tested per tissue, were considered significantly enriched for genes associated with a given trait. To  
822 test the specificity of ECLIPSER, we applied the method to eight negative control traits listed in  
823 Supplementary Table 45. To assess the robustness of the cell type enrichment results with  
824 ECLIPSER, we ran two additional cell type enrichment methods of GWAS data that consider  
825 genome-wide genetic associations beyond genome-wide significant loci: stratified LD score  
826 regression<sup>25</sup> and MAGMA<sup>107</sup> (see below).

827  
828 **Cell type specific heritability enrichment of disease associations using stratified LD score**  
829 **regression.** We applied stratified LD score regression (S-LDSC)<sup>25</sup> (v1.0.1; URLs) to the GWAS  
830 summary statistics of the POAG cross-ancestry meta-analysis, POAG European subset meta-  
831 analysis and IOP meta-analysis, and the four single-nucleus differential gene expression datasets  
832 described above, to evaluate the contribution of genetic variation in cell type-specific genes to trait  
833 heritability. Common variants (MAF>1%) within or near genes specifically expressed in the different  
834 cell types (fold-change > 1.1 and FDR<0.1) in each of the four single-nucleus eye tissue datasets  
835 described above, were considered in the S-LDSC analysis. A 100 kb windows on either side of  
836 each gene was used. The European samples in 1000 Genomes Project Phase 3<sup>96</sup> were used as  
837 the reference panel for computing the LD scores for all three GWAS meta-analyses. Heritability  
838 enrichment per cell type was considered significant at Benjamini-Hochberg FDR below 0.1.

839  
840 **MAGMA gene-association correlation with cell type gene expression.** We applied the  
841 regression-based model MAGMA (v1.10)<sup>107</sup> to the POAG cross-ancestry, POAG European subset,  
842 and IOP GWAS meta-analyses and the four single-nucleus ocular expression datasets described  
843 above, which tests for association between gene association z-scores and average gene  
844 expression per cell type, controlling for average gene expression across all cell types per tissue.  
845 Gene-based association z-scores were computed for each GWAS based on the most significant  
846 variant (SNP-wise=top) within 100kb around each gene, as described in de Leeuw *et al.*<sup>108</sup>. The

847 European samples in 1000 Genomes Project Phase 3<sup>96</sup> were used as the reference panel for the  
848 POAG EUR and IOP GWAS, while all five populations (EUR, AFR, AMR, EAS, SAS) were used  
849 for the POAG cross-ancestry GWAS. Significance was determined at Benjamini-Hochberg FDR  
850 below 0.1. We applied conditional analysis to all pairwise combinations of nominally significant  
851 (P<0.05) cell types within a given tissue, to identify cell types whose trait association signals are  
852 independent of the other significant cell type<sup>107</sup>. A proportional significance (PS) of the conditional  
853 P-value of a cell type relative to its marginal P-value was computed for each cell type in each cell  
854 type pair. Two cell types in a given pair with PS $\geq$ 0.8 were considered independently associated  
855 cell types, and a pair of cell types with PS $\geq$ 0.5 were considered partial-joint associations. In the  
856 case where one cell type had PS $\geq$ 0.5 and the second cell type a conditional P-value  $\geq$ 0.05, the  
857 first cell type was retained and the second cell type was considered completely dependent on the  
858 association of the first cell type. For more details see: <https://fuma.ctglab.nl/tutorial#celltype>.

859  
860 **Gene set enrichment analysis of POAG and IOP associated genes.** We used *GeneEnrich*<sup>24,26</sup>  
861 to test whether genes proposed to affect POAG risk or IOP variation cluster in specific biological  
862 processes or mouse phenotype ontologies. *GeneEnrich* assesses enrichment of a set of genes of  
863 interest in biological pathways or other types of biologically meaningful gene sets, using a  
864 hypergeometric distribution and permutation analysis. To account for biases that could arise from  
865 the set of genes expressed in a given tissue, an empirical gene set enrichment P-value was  
866 computed as the fraction of 1,000 to 100,000  $k$  randomly sampled genes ( $k$  = number of significant  
867 genes, e.g., colocalizing e/sGenes) from all genes expressed in the given tissue (background set)  
868 that have a hypergeometric probability equal to or higher than that of the significant list of genes.  
869 Given the high LD in the HLA region on chromosome 6 (chr6:28510120-33480577) we removed  
870 all genes in this region from the gene set enrichment analysis, unless noted otherwise.

871 We applied *GeneEnrich* to three groups of POAG and IOP associated genes: (i) All 228,  
872 118, and 279 unique target genes of eQTLs and sQTLs that colocalized with POAG cross-ancestry,  
873 POAG EUR, and IOP GWAS loci, respectively. Given that the colocalizing e/sQTLs were derived  
874 from the different GTEx tissues and retina, we used all genes expressed in any of the 49 GTEx  
875 tissues and retina as the background set of genes, and did not correct for expression levels given  
876 the differences in expression levels between the tissues. (ii) Sets of POAG and IOP colocalizing  
877 genes that were enriched in specific cell types in the eye tissues based on ECLIPSER analysis  
878 (tissue-wide FDR  $\leq$  0.1). For the background sets of genes, we chose all genes expressed in the  
879 GTEx or retina tissue that was most relevant for the enriched cell type (e.g., Brain for Optic nerve  
880 head; full list in Supplementary Table 39). Given that the expression levels in a tissue may not fully

881 reflect the expression levels in the particular cell type, we did not correct for expression levels in  
882 the gene set enrichment analysis of the cell type-specific gene sets. (iii) Target genes of e/sQTLs  
883 (FDR<0.05) with top ranked POAG or IOP GWAS P-values ( $P < 0.05$ ) in tissues whose e/sQTLs  
884 were enriched for trait associations based on *QTLEnrich*. Given that e/sQTLs in most tissues  
885 displayed significant enrichment, a selected set of QTL/tissue-trait pairs was chosen for gene set  
886 enrichment analysis based on the tissue having a top ranked adjusted fold-enrichment and  
887 consisting of cell types that may be relevant to glaucoma pathophysiology, such as cells cultured  
888 fibroblasts, brain, and artery (Supplementary Tables 4-5). The background sets of genes were  
889 defined as all genes expressed in the given tissue excluding the target genes of e/sQTLs with  
890 GWAS  $P < 0.05$ . The expression levels of the randomly sampled genes from the background set in  
891 the permutation analysis were matched on the expression levels of the significant set of genes.

892 We applied *GeneEnrich* to over 11,000 gene sets from four databases downloaded from  
893 MSigDB (URLs): Gene Ontology (GO) with three domains: biological processes, molecular  
894 function, and cellular components; Reactome; Kyoto Encyclopedia of Genes and Genomes  
895 (KEGG); and mouse phenotype ontology gene sets from the Mouse Genome Informatics (MGI).  
896 Only gene sets with 10 to 1000 genes were tested, and only genes that were found in the given  
897 database were included in the analysis. Statistical significance was determined using a Benjamini  
898 Hochberg FDR below 0.1 per database, given extensive gene set overlap between databases.  
899 Gene sets with empirical gene set enrichment below 0.05 were considered nominally significant.  
900

901 **Conditional analysis of *MYOC* POAG locus.** Given our finding of significant colocalization of a  
902 *P/GC* sQTL with the POAG cross-ancestry association signal in the GWAS locus rs74315329,  
903 whose lead variant is a nonsense mutation in the *MYOC* gene, we tested whether there was a  
904 secondary independent signal in this locus that might colocalize with the *P/GC* sQTL. We  
905 performed association testing on all variants on chromosome 1 conditioning on rs74315329, the  
906 lead POAG GWAS variant in the locus by applying the tool COJO (URLs) to the POAG cross-  
907 ancestry GWAS meta-analysis summary statistics on chromosome 1. To maintain the *MYOC* lead  
908 variant in the initial association testing we filtered out variants with  $MAF < 0.0001$ . The effective  
909 sample size of the POAG cross-ancestry GWAS was computed based on the equation:  
910  $4/[(1/N_{\text{cases}})+(1/N_{\text{controls}})]^{109}$ , which yielded  $N=124,531$  for the POAG GWAS cross-ancestry  
911 meta-analysis<sup>8</sup>. For the variant allele frequencies required as input to COJO, we used the  
912 European, African and East Asian samples in 1000 Genomes Project<sup>96</sup>, as the POAG GWAS meta-  
913 analysis is comprised of these three ancestral groups. eCAVIAR and *enloc* were applied to the  
914 residual statistics in the *MYOC* locus from the conditional analysis and all overlapping e/sQTLs

915 from the GTEx tissues and retina. To remove potential false positives, we filtered out variant, gene,  
916 tissue, trait combinations if the e/sVariant with a significant colocalization result had a GWAS p-  
917 value above  $2 \times 10^{-5}$  or an e/sQTL p-value above  $1 \times 10^{-4}$  and/or an FDR above 0.05 (FALSE in  
918 column 'Pass\_QC\_QTL\_FDR05\_P1E04\_GWAS\_P2E05' in Supplementary Tables 25 and 27). We  
919 used a slightly more lenient GWAS p-value cutoff for the conditional analysis ( $P < 2 \times 10^{-5}$  compared  
920 to  $P < 1 \times 10^{-5}$  used for the original GWAS summary statistics) given the reduced association power  
921 of conditional analysis.

922

### 923 **Data availability**

924 All GTEx protected data are available through the database of Genotypes and Phenotypes (dbGaP)  
925 (accession no. phs000424.v8). The GTEx eQTL and sQTL and EyeGEx retina eQTL summary  
926 statistics are available on the GTEx portal (<https://gtexportal.org/home/datasets>). The snRNA-seq  
927 data for the anterior segment and macula are available in Gene Expression Omnibus (GEO)  
928 accession number GSE199013, for the optic nerve head and posterior tissues in GSE236566, and  
929 for the retina in GSE226108. The processed data of the anterior and posterior segments can be  
930 visualized in the Broad Institute's Single Cell Portal at  
931 [https://singlecell.broadinstitute.org/single\\_cell/study/SCP1841](https://singlecell.broadinstitute.org/single_cell/study/SCP1841) and  
932 [https://singlecell.broadinstitute.org/single\\_cell/study/SCP2298](https://singlecell.broadinstitute.org/single_cell/study/SCP2298). The retina Hi-C data is accessible  
933 in GEO accession number GSE202471. The GWAS summary statistics for the POAG cross-  
934 ancestry GWAS meta-analysis and European subset meta-analysis are accessible in GEO under  
935 accession numbers GCST90011770 and GCST90011766, respectively, and for IOP are available  
936 from the corresponding publication (Khawaja *et al.*, Nature Genetics 2018). The GWAS loci for  
937 complex traits analyzed in this study were downloaded from Open Targets Genetics  
938 (<https://genetics.opentargets.org/>). The gene sets taken from MSigDB were downloaded from:  
939 <http://www.gsea-msigdb.org/gsea/msigdb/collections.jsp>, and the mouse phenotype ontology gene  
940 sets from the Mouse Genome Informatics (MGI) website (<http://www.informatics.jax.org/>).

941

### 942 **Code Availability**

943 The code of all tools used for analyses in this paper are publicly available and are listed in the URLs  
944 below. Custom code used to generate some of the plots are available upon request.

945

### 946 **URLs**

947 GTEx: <https://gtexportal.org/home/datasets>

948 EyeGEx: <https://gtexportal.org/home/datasets>

949 QTLEnrich v2: <https://github.com/segrelabgenomics/QTLEnrich>  
950 GeneEnrich v2: <https://github.com/segrelabgenomics/GeneEnrich>  
951 MSigDB: <http://www.gsea-msigdb.org/gsea/msigdb/collections.jsp>  
952 PLINK: <https://www.cog-genomics.org/plink/>  
953 eCAVIAR: <https://github.com/fhormoz/caviar>  
954 fastEnloc: <https://github.com/xqwen/fastenloc>  
955 DAP-G: [https://github.com/xqwen/dap/tree/master/dap\\_src](https://github.com/xqwen/dap/tree/master/dap_src)  
956 ECLIPSER: <https://github.com/segrelabgenomics/ECLIPSER>  
957 MAGMA v1.10: <https://ctg.cncr.nl/software/magma>, <https://fuma.ctqlab.nl/tutorial#celltype>  
958 S-LDSC v1.0.1: <https://github.com/bulik/ldsc>  
959 genomAD: <https://gnomad.broadinstitute.org/>  
960 QMplot: <https://github.com/ShujiaHuang/qmplot>  
961 LocusCompare: <https://github.com/boxiangliu/locuscomparer>  
962

### 963 **Acknowledgements**

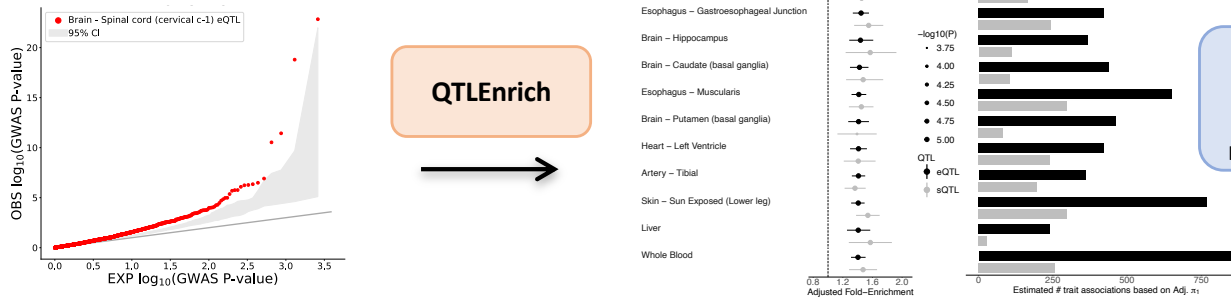
964 We thank William Wen for helpful discussions on the interpretation of the colocalization results. We  
965 thank members of the Segrè lab for valuable comments and feedback. This work was funded by  
966 NIH/NEI R01 EY031424-01 (AVS, ARH, JR, PAM), NIH/NEI P30 EY014104 (JLW, AVS), NIH/NEI  
967 EY032559-01 (JLW, AVS), and the Chan Zuckerberg Initiative (CZI) Seed Network for the Human  
968 Cell Atlas awards CZF2019-002459 (JRS, AVS, WY, AM) and CZF2019-002425 (QL, RC). XJ is  
969 supported by the University of Edinburgh and University of Helsinki joint PhD studentship program  
970 in Human Genomics. VV is supported by an MRC University Unit Programme grant  
971 (MC\_UU\_00007/10) (QTL in Health and Disease). APK is supported by a UK Research and  
972 Innovation Future Leaders Fellowship, an Alcon Research Institute Young Investigator Award and  
973 a Lister Institute for Preventive Medicine Award. This research was supported by the NIHR  
974 Biomedical Research Centre at Moorfields Eye Hospital and the UCL Institute of Ophthalmology.  
975

### 976 **Competing interests**

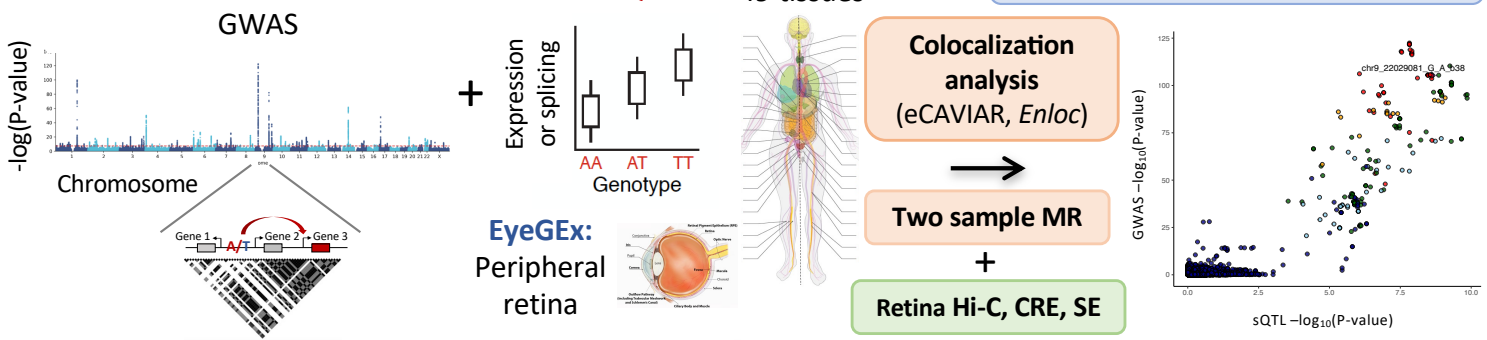
977 APK has acted as a paid consultant or lecturer to Abbvie, Aerie, Allergan, Google Health,  
978 Heidelberg Engineering, Novartis, Reichert, Santen and Thea.  
979  
980  
981  
982

**Figure 1**

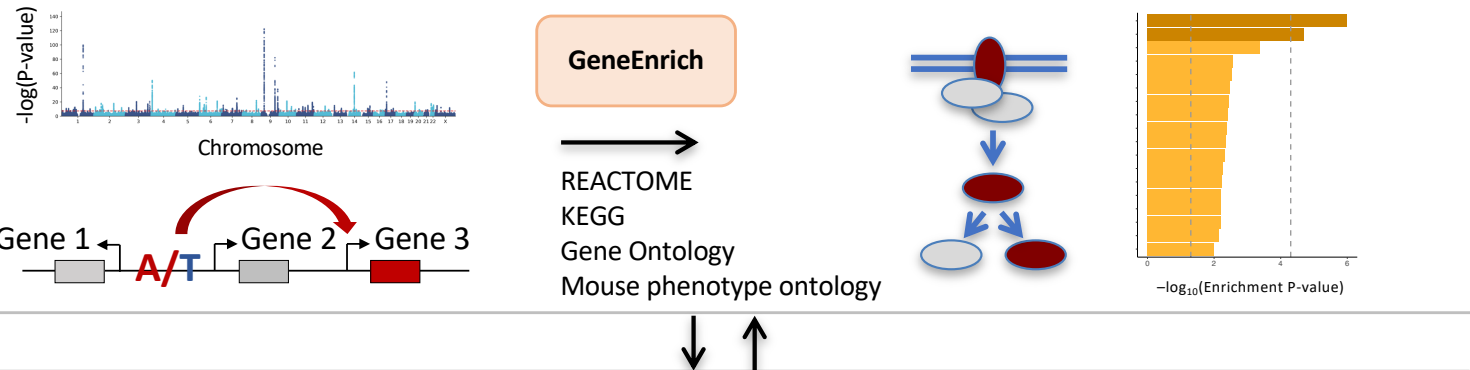
**a. Enrichment of POAG or IOP associations among e/sQTLs in GTEx tissues and retina**



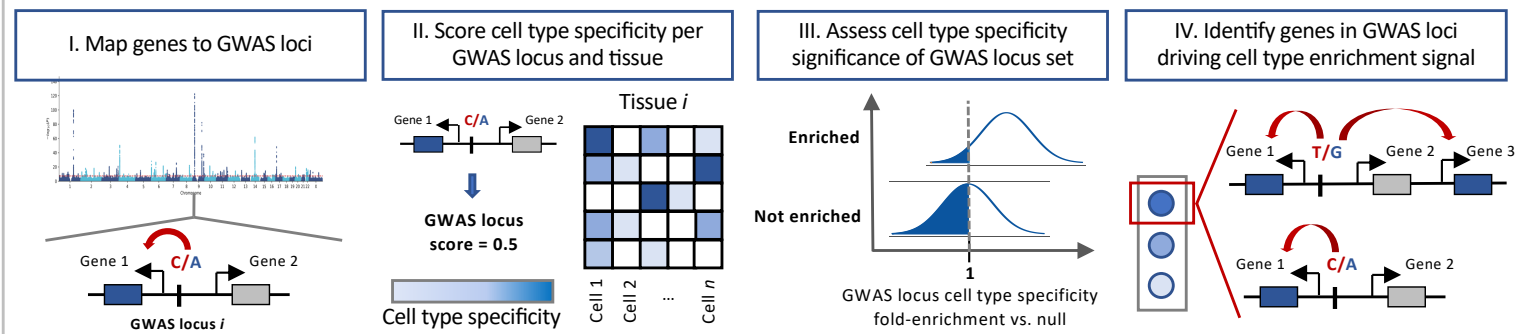
**b. Mapping genes to GWAS loci**



**c. Gene set enrichment of colocalizing genes and cell type specific genes**



**d. Cell type enrichment of e/sQTL-mapped genes in GWAS loci in ocular tissues**



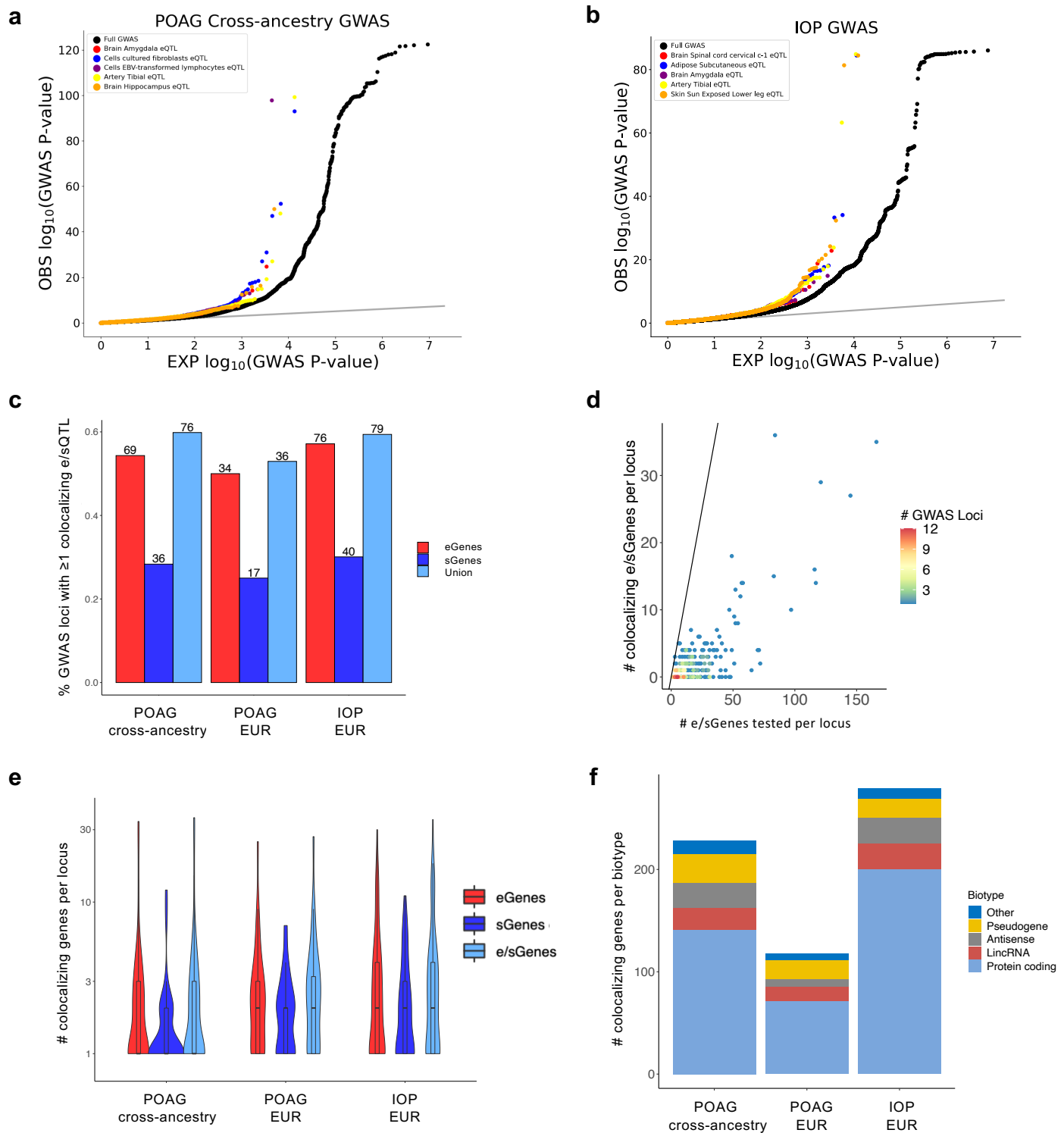
**e. Genome-wide association enrichment in ocular cell types and conditional analysis**



1016 **Figure 1. Analysis workflow from POAG and IOP GWAS to causal regulatory mechanisms,**  
1017 **genes, pathways, and cell types.** **a**, POAG and IOP associations genome-wide (known and  
1018 modest associations) were tested for enrichment among e/sQTLs in GTEx tissues and retina  
1019 compared to permuted null sets of variants matched on confounding factors, using *QTLEnrich*. In  
1020 cases where enrichment was found, the lower bound number of e/sQTLs in a given tissue, likely to  
1021 be true trait associations was estimated using an empirically derived, true positive rate ( $\pi_1$ )  
1022 approach. **b**, Putative causal genes were prioritized per known POAG and IOP GWAS locus by  
1023 applying two colocalization methods to all e/sQTLs from 49 GTEx tissues and retina eQTLs that  
1024 overlapped each locus. A Manhattan plot of the POAG cross-ancestry GWAS meta-analysis was  
1025 plotted with QMplot (URLs). **c**, All target genes of significantly colocalizing e/sQTLs per trait were  
1026 tested for enrichment in signaling and metabolic pathways (Reactome, KEGG), gene ontologies  
1027 and mouse phenotype ontologies using *GeneEnrich*. **d**, Significantly colocalizing e/sGenes were  
1028 tested for enrichment in specific cell types in single nucleus RNA-seq data of glaucoma-relevant  
1029 eye tissues, using ECLIPSER. Cell type specific genes were defined with cell type fold-change  
1030  $>1.3$  and  $FDR<0.1$  per tissue. Cell type specificity significance per GWAS locus set for a given trait  
1031 was assessed against a null distribution of GWAS loci associated with unrelated, non-ocular traits,  
1032 using a Bayesian Fisher's exact test. Genes mapped to GWAS loci with a cell type specificity score  
1033 above the 95th percentile of null locus scores were proposed as contributing to the trait in the  
1034 enriched cell type. **e**, Cell type enrichment for the POAG and IOP GWAS was corroborated using  
1035 two regression-based methods that assess cell type specificity of trait associations considering all  
1036 associations genome-wide: stratified-LD score regression and MAGMA.

1037  
1038  
1039  
1040  
1041  
1042  
1043  
1044  
1045  
1046  
1047  
1048  
1049

**Figure 2**



1083 **Figure 2. Enrichment and colocalization analysis of eQTLs and sQTLs with POAG and IOP**  
1084 **associations.** **a, b** Quantile-quantile (Q-Q) plots of POAG cross-ancestry (**a**) and IOP (**b**) GWAS  
1085  $-\log_{10}$  (P-value) compared to expectation for the best eQTL per eGene sets (eVariants with FDR <  
1086 0.05) of the top enriched tissues based on adjusted fold-enrichment (colored points), compared to  
1087 all variants in the GWAS (black points). Grey line represents the diagonal. **c**, Histogram of percent  
1088 of GWAS loci with at least one colocalizing e/sQTL (eCAVIAR CLPP > 0.01 and/or *enloc* RCP >  
1089 0.1) for the three traits (POAG cross-ancestry, POAG European (EUR) ancestry subset, and IOP  
1090 European ancestry). Numbers above the bars represent the number of loci with at least one  
1091 colocalizing e/sQTL. Red, dark blue, and light blue bars indicate percentage of loci with at least  
1092 one colocalizing eGene, sGene, or both, respectively. **d**, Scatter plot comparing unique number of  
1093 e/sGenes per locus that significantly colocalized per locus versus unique number of e/sGenes  
1094 tested per locus. Points are color-coded by number of GWAS loci. The black line represents the  
1095 diagonal. **e**, Violin plots showing the distribution of the unique number of colocalizing eGenes (red),  
1096 sGenes (dark blue), or both (light blue) per locus for the three GWAS tested. The center line in the  
1097 box plots contained within each violin plot shows the median and the box edges depict the  
1098 interquartile range. **f**, Stacked histogram showing the number of colocalizing e/sGenes per gene  
1099 biotype for each GWAS. Protein coding (light blue), lincRNA (brown), antisense (grey),  
1100 pseudogenes (yellow), and other (dark blue).

1101

1102

1103

1104

1105

1106

1107

1108

1109

1110

1111

1112

1113

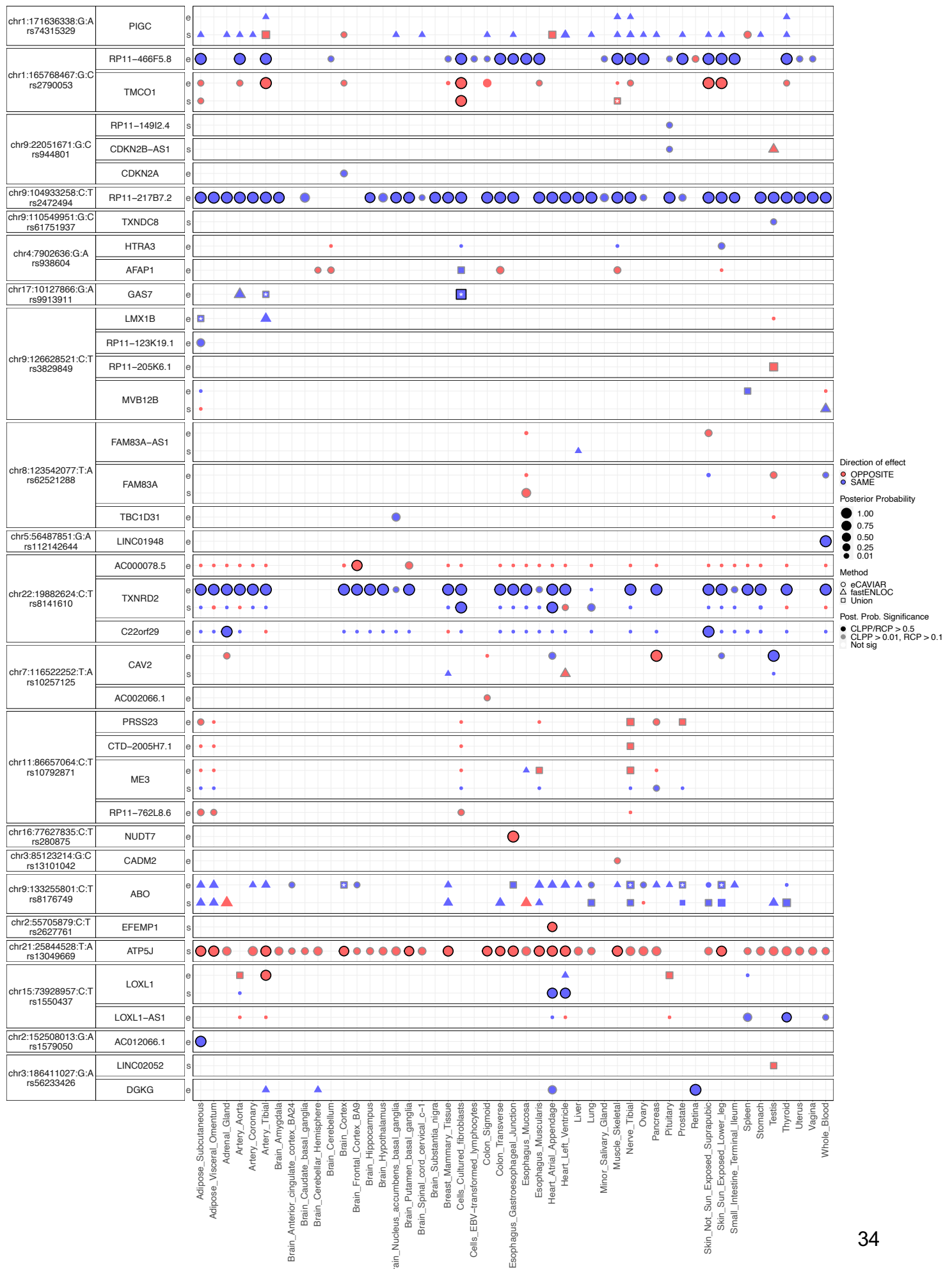
1114

1115

1116

**Figure 3**

Top POAG cross-ancestry GWAS loci



1150 **Figure 3. Colocalizing e/sQTLs in GTEx tissues and retina with top POAG GWAS loci.** Genes  
1151 with at least one significant colocalization result are shown for e/sQTLs tested across 49 GTEx  
1152 tissues and peripheral retina for the top 21 POAG cross-ancestry GWAS loci. GWAS loci were  
1153 ordered by absolute value of their effect size. Within each locus, genes were ordered based on  
1154 their chromosome position. Bubble size is proportional to the maximum colocalization posterior  
1155 probability of all e/sVariants tested for the given gene, QTL type and tissue combination. Points are  
1156 color-coded by direction of effect (blue if increased expression or splicing increases POAG risk or  
1157 vice versa; red if increased expression or splicing decreases POAG risk or vice versa). Shape of  
1158 points indicates colocalization method used: circle (eCAVIAR), triangle (*en/loc*), and square (tested  
1159 in both methods; results shown for method with maximum posterior probability). Grey or black  
1160 border denotes variant-gene-tissue-QTL combination that passed QC filtering (Methods) and a  
1161 colocalization posterior probability cutoff above 0.01/0.1 (CLPP/RCP) or 0.5 (higher confidence),  
1162 respectively. White or black asterisk in the square indicates whether the second method tested  
1163 passed a posterior probability cutoff 0.01/0.1 (CLPP/RCP) or 0.5, respectively.

1164

1165

1166

1167

1168

1169

1170

1171

1172

1173

1174

1175

1176

1177

1178

1179

1180

1181

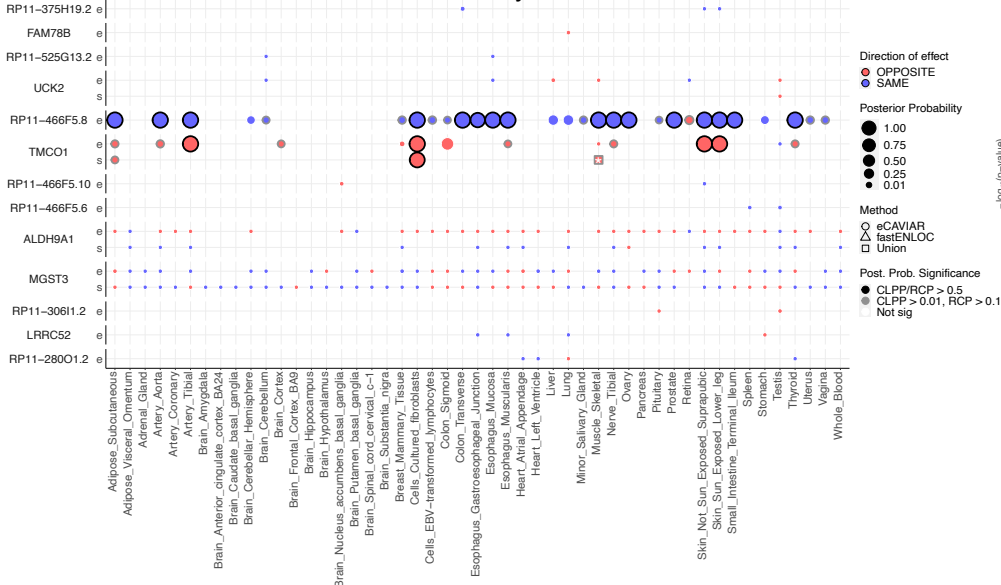
1182

1183

**Figure 4**

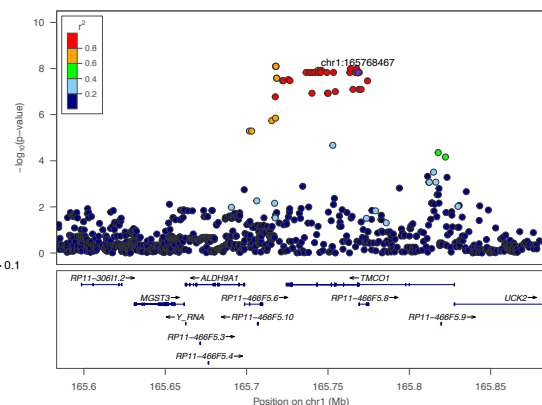
**a**

POAG cross-ancestry locus rs2790053



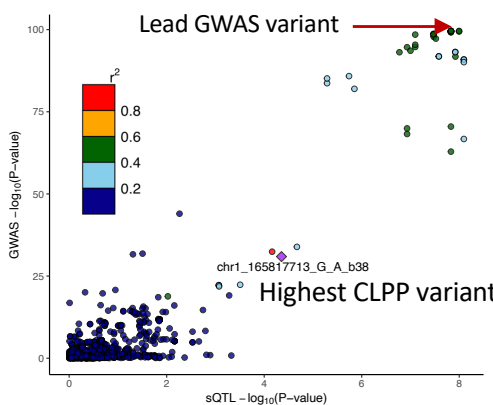
**b**

TMCO1 Cells cultured fibroblast sQTL



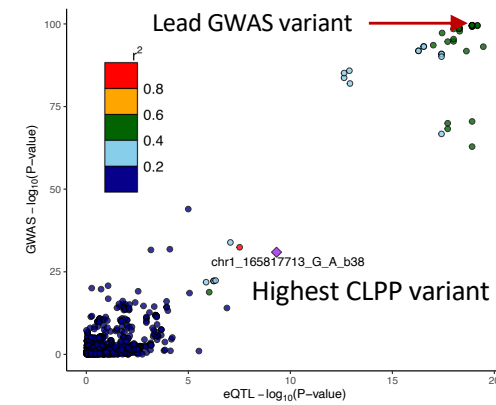
**c**

TMCO1 Cultured fibroblast sQTL (CLPP=0.92)



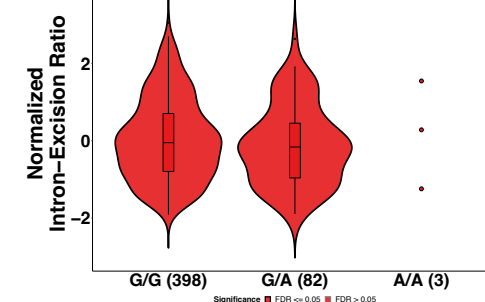
**d**

RP11-466F5.8 Cultured Fibroblast eQTL (CLPP=1)



**e**

Cells Cultured Fibroblasts  
chr1\_165817713\_G\_A\_b38  
TMCO1, ENSG0000143183.16  
chr1:165768269:165768482:clu\_45311  
p-val = 4.42e-05, beta= -4.3e-01

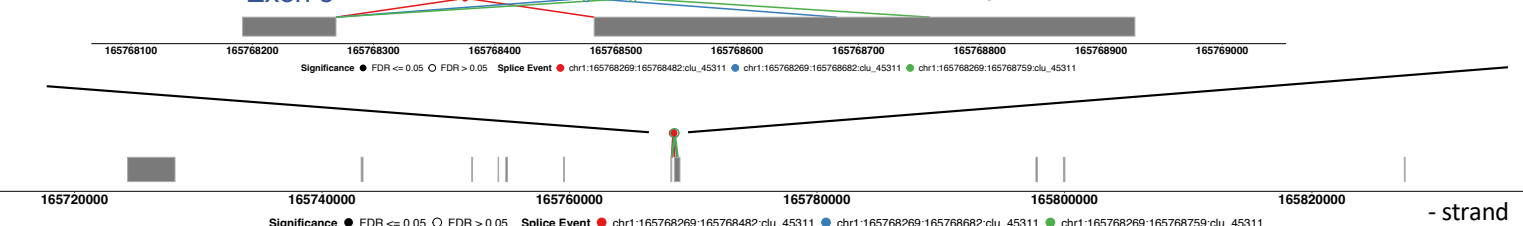


**f**

TMCO1

Exon 5

Exon 4

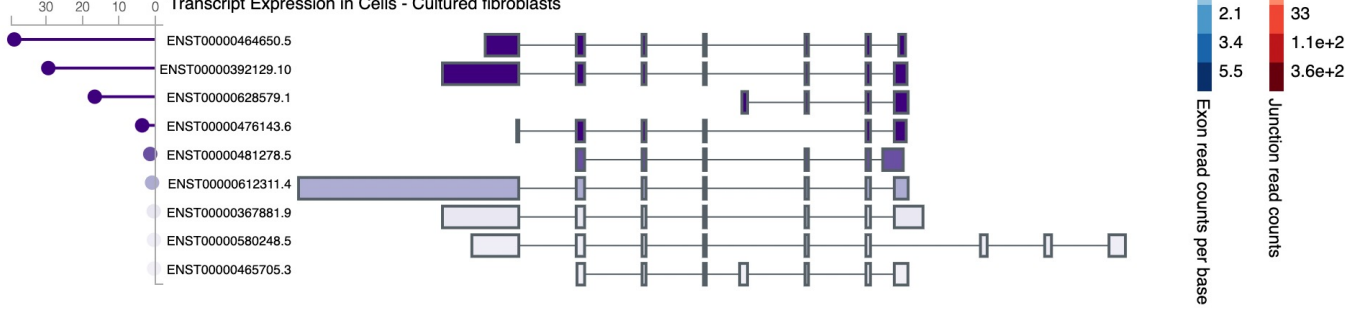


**g**

TMCO1

Gene Model

Transcript Expression in Cells - Cultured fibroblasts



1217 **Figure 4. Examples of colocalizing e/sQTLs with top POAG and IOP GWAS loci. a,**  
1218 Colocalization results for all e/sGenes tested in the POAG cross-ancestry rs2790053 locus LD  
1219 interval with  $\geq 1$  significant eQTL or sQTL result across 49 GTEx tissues and peripheral retina based  
1220 on eCAVIAR and/or *en/loc*. Genes were ordered by chromosome position. Size of points is  
1221 proportional to the maximum colocalization posterior probability of all e/sVariants tested for the  
1222 given gene, QTL type and tissue combination. Points are color-coded by direction of effect (blue if  
1223 increased expression or splicing increases POAG risk or vice versa; red if increased expression or  
1224 splicing decreases POAG risk or vice versa). Shape of points indicates colocalization method: circle  
1225 (eCAVIAR), triangle (*en/loc*), and square (tested in both methods; results shown for method with  
1226 maximum posterior probability). Grey or black border denote variant-gene-tissue-QTL combination  
1227 that passed QC filtering (Methods) and a colocalization posterior probability cutoff above 0.01/0.1  
1228 (CLPP/RCP) or 0.5, respectively. White or black asterisk in the square indicates whether the  
1229 second method tested passed a posterior probability cutoff of 0.01/0.1 (CLPP/RCP) or 0.5,  
1230 respectively. **b**, LocusZoom<sup>96</sup> plot for *TMCO1* sQTL  $-\log_{10}(P\text{-value})$  in GTEx Cells Cultured  
1231 fibroblasts in the POAG cross-ancestry GWAS variant rs2790053 (chr1\_165768467\_C\_G\_b38) LD  
1232 interval. Points are color-coded by LD ( $r^2$ ) relative to the lead GWAS variant. **c,d** LocusCompare  
1233 plot of  $-\log_{10}(P\text{-value})$  of the POAG cross-ancestry GWAS meta-analysis versus the  $-\log_{10}(P\text{-value})$   
1234 of the Cells Cultured fibroblast sQTL or eQTL acting on *TMCO1* (**c**) or *RP11-466F5.8* (**d**),  
1235 respectively. Points are color-coded based on LD ( $r^2$ ) relative to the variant with the highest  
1236 eCAVIAR colocalization posterior probability (CLPP). **e**, Violin plot of normalized intron-excision  
1237 ratio for chr1:165768269-165768482 computed with Leafcutter<sup>95</sup> for *TMCO1* in Cells Cultured  
1238 fibroblasts as a function of the genotype of the sVariant chr1\_165817713\_G\_A\_b38 (rs143863391)  
1239 with the highest CLPP (0.92) for this sQTL and the POAG cross-ancestry GWAS locus rs2790053.  
1240 The effect size of the sQTL relative to the alternative allele (*beta* = -0.43) is in opposite direction  
1241 relative to the GWAS variant (*beta* = 0.25), suggesting that decreased splicing between  
1242 chr1:165768269-165768482 increases POAG risk. **f**, Gene model for *TMCO1* in GTEx fibroblasts  
1243 on the negative strand showing all intron excision splicing events detected with Leafcutter in  
1244 *TMCO1*. A zoom in of the splicing event (chr1:165768269-165768482; red), an alternative splice  
1245 donor site on exon 4 (red versus blue or green), associated with the sVariant  
1246 chr1\_165817713\_G\_A\_b38 that colocalized with POAG risk is shown. A longer exon 4 in *TMCO1*  
1247 is associated with decreased risk of POAG. **g**, *TMCO1* gene model and transcripts expressed in  
1248 Cells Cultured fibroblasts taken from the GTEx portal (URLs). In the gene model, exon boxes are  
1249 color-coded by exon read counts per base (blue) and lines connecting exons are color-coded by  
1250 exon-exon junction read counts (red). All splicing events observed in the tissue are shown,

1251 including the alternative splice event between exon 4 and exon 5 whose genetic regulation  
1252 colocalized with POAG (c). Below the gene model, transcript expression in Cells Cultured  
1253 fibroblasts in Transcripts per Million (TPM), computed with RSEM<sup>110</sup>, is shown in descending order.

1254

1255

1256

1257

1258

1259

1260

1261

1262

1263

1264

1265

1266

1267

1268

1269

1270

1271

1272

1273

1274

1275

1276

1277

1278

1279

1280

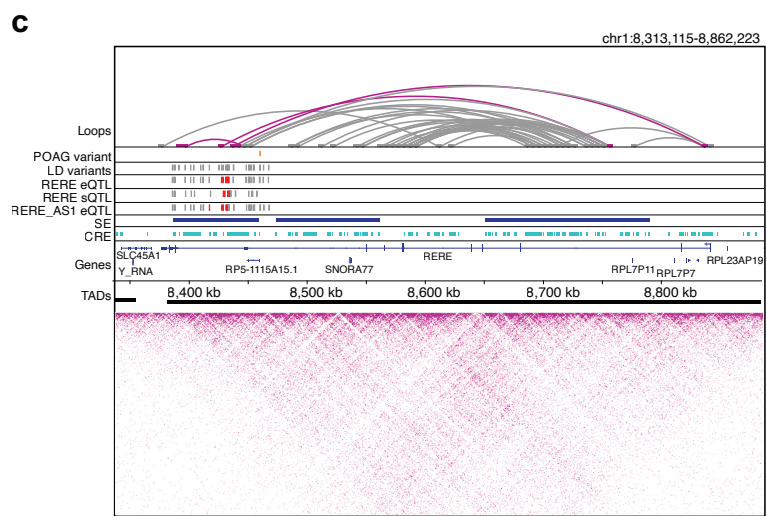
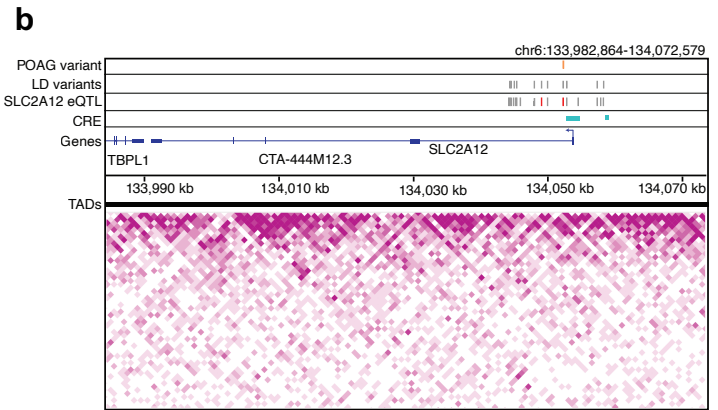
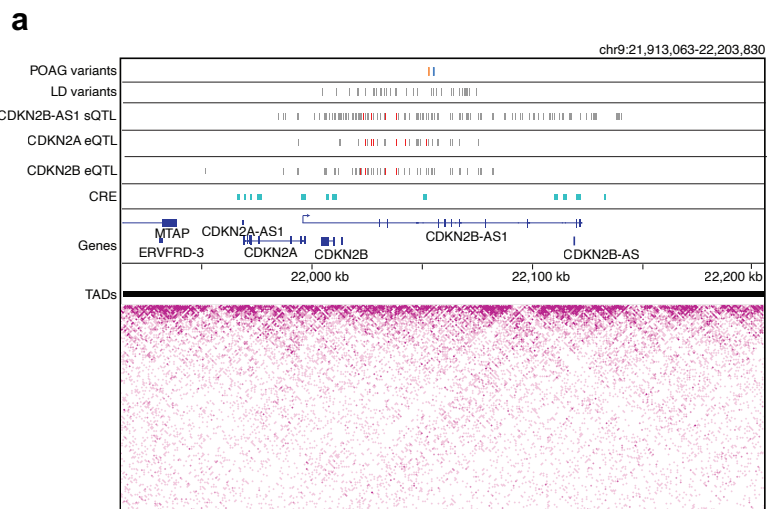
1281

1282

1283

1284

**Figure 5**



1318 **Figure 5. Chromatin loops and regulatory elements in human retina support effect of**  
1319 **colocalizing e/sQTLs on POAG risk. a**, Retina CREs (cyan) derived from epigenetic data  
1320 overlapping e/sVariants that colocalized with POAG associations in the *CDKN2A/B* locus. The lead  
1321 POAG variants from the cross-ancestry (blue line) and European subset (orange line) GWAS are  
1322 shown in the top track, followed by their linkage disequilibrium (LD) proxy variants ( $r^2>0.8$ ) in the  
1323 track below. The significantly colocalizing *CDKN2B-AS1* sVariants in Pituitary, *CDKN2A* eVariants  
1324 in Brain Cortex, and *CDKN2B* eVariants in Skeletal Muscle are represented by red lines, and the  
1325 grey lines represent LD proxy variants that are also significant e/sQTLs (FDR<0.05) for the  
1326 corresponding gene and tissue. **b**, Retina CREs (cyan) overlapping retina *SLC2A12* eVariants that  
1327 colocalized with the POAG cross-ancestry association. Tracks display the lead POAG cross-  
1328 ancestry GWAS variant (orange) and its LD proxy variants (grey), followed by the significantly  
1329 colocalizing *SLC2A12* retina eVariants (red) with their LD proxy eVariants that are also significant  
1330 eQTLs at FDR<0.05 (grey). The CRE overlaps the promoter of *SLC2A12*. **c**, Retina chromatin loops  
1331 from Hi-C data, SEs (blue), and CREs (cyan) shown for the *RERE* POAG locus. Tracks display the  
1332 lead POAG cross ancestry GWAS variant (orange) and its LD proxy variants (grey), followed by  
1333 significantly colocalizing *RERE* eVariants in Nerve Tibial, *RERE* sVariants in fibroblast cells, and  
1334 *RERE-AS1* eVariants in Adipose Subcutaneous (red), and their LD proxy variants that are also  
1335 significant e/sQTLs (FDR<0.05) for the corresponding gene and tissue (grey). Magenta loops have  
1336 one foot that overlaps or is in LD with the POAG variant and colocalizing e/sQTLs. In all panels,  
1337 LD proxy variants were computed at  $r^2>0.8$ , TADs are represented as solid black lines, and the  
1338 magenta heatmaps represent Hi-C physical contact maps. CRE, Cis-regulatory element; SE,  
1339 Super-enhancer; TAD, Topologically associating domain.

1340

1341

1342

1343

1344

1345

1346

1347

1348

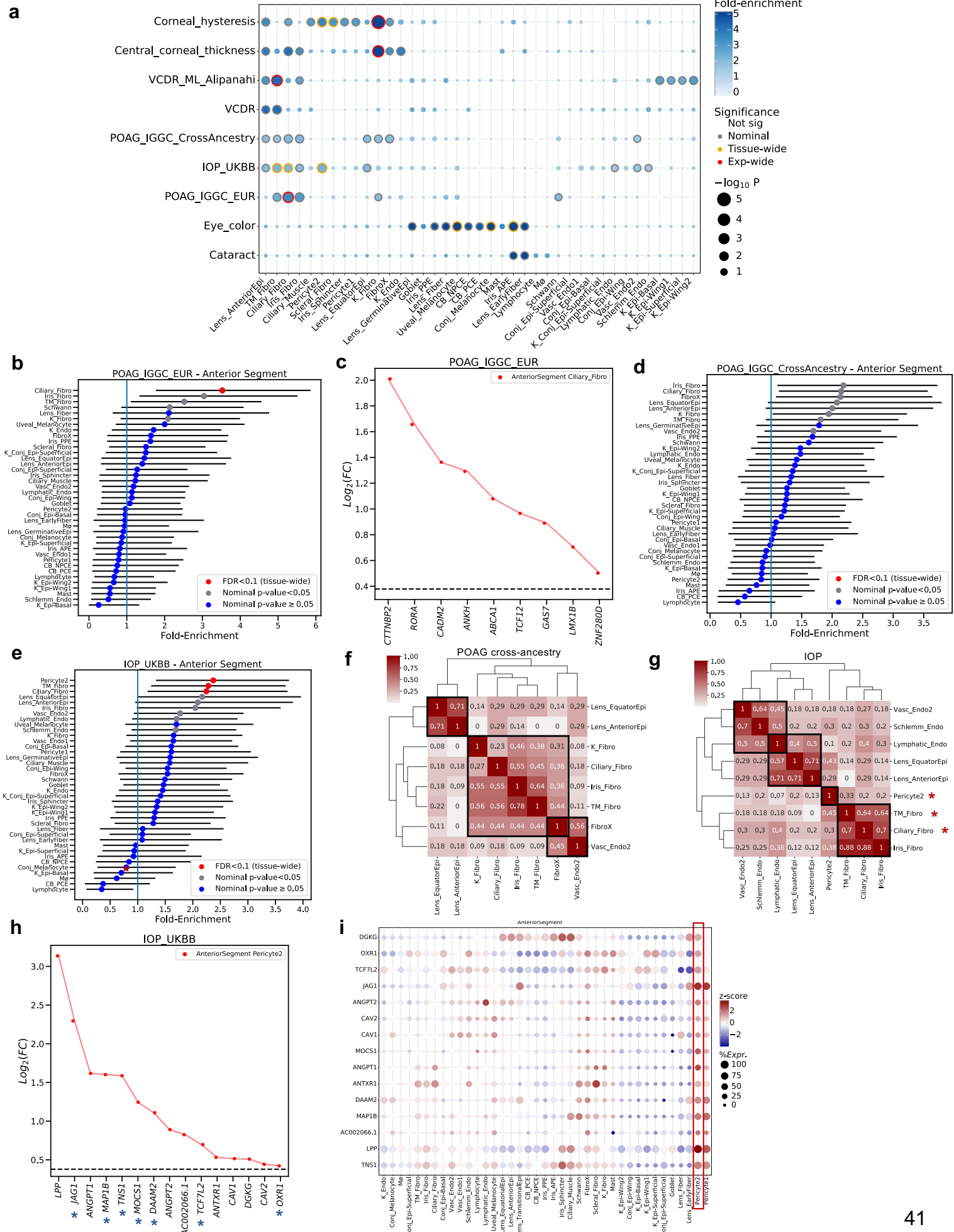
1349

1350

1351

**Figure 6**

## Anterior Segment



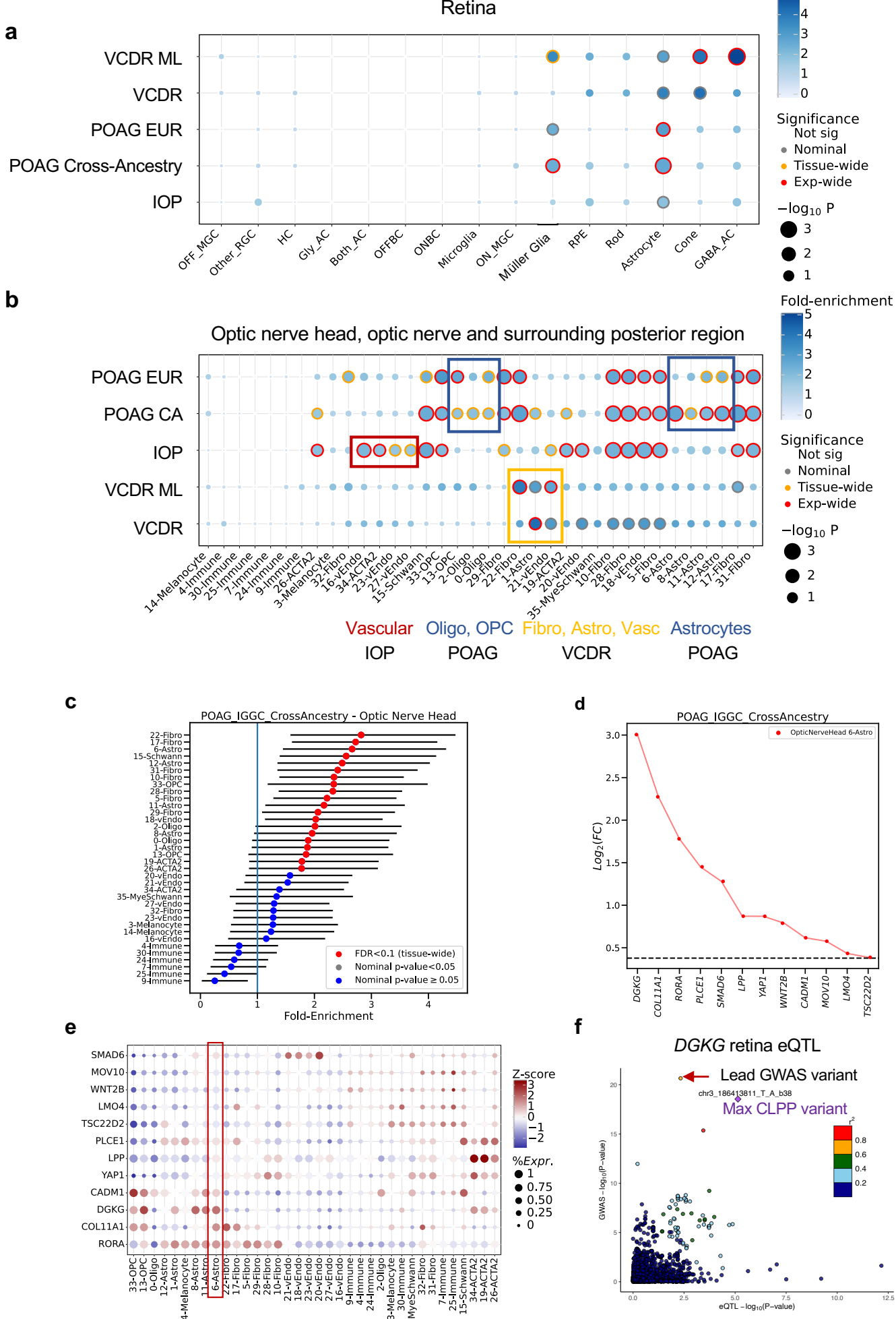
1385 **Figure 6. Cell type enrichment of e/sQTL-mapped genes for POAG, IOP and related trait loci**  
1386 **in the anterior segment of the eye.** **a**, Significance (circle size,  $-\log_{10}(P\text{-value})$ ) and fold-  
1387 enrichment (circle color) of the cell type specificity of GWAS locus sets for POAG cross-ancestry,  
1388 POAR European subset, IOP, central cornea thickness, corneal hysteresis, physician-defined  
1389 vertical-cup-to-disc ratio (VCDR), and machine learning (ML)-defined VCDR  
1390 (VCDR<sub>ML</sub>\_Alipanahi) are shown for each of the 39 cell types found in six tissues in the anterior  
1391 segment of the eye<sup>36</sup>. Traits (rows) and cell types (columns) were clustered based on hierarchical  
1392 clustering of the euclidean distance between GWAS locus set cell type-specificity enrichment  
1393 scores. Red rings: experiment-wide significant (Benjamini Hochberg (BH) FDR<0.1); Yellow rings:  
1394 tissue-wide significant (BH FDR<0.1); Grey rings: nominal significant ( $P<0.05$ ). **b,d,e**, Cell type  
1395 specificity fold-enrichment (x-axis) in the different anterior segment cell types ranked in descending  
1396 order for the POAG European subset (**b**), POAG cross-ancestry (**d**), and IOP (**e**) GWAS locus sets.  
1397 Error bars: 95% confidence intervals. Red: tissue-wide significant (FDR<0.1); Grey: nominal  
1398 significant ( $P<0.05$ ); Blue: non-significant ( $P\geq 0.05$ ). **c,h**, Differential gene expression ( $\log_2(\text{Fold-}$   
1399 change), y axis) in the most strongly enriched cell type compared to all other cell types is shown  
1400 for the set of genes (x axis) driving the enrichment signal of the POAG European GWAS loci in  
1401 ciliary fibroblasts (**c**) and the IOP GWAS loci in pericytes (cluster 2) (**h**). Vertical dashed line  
1402 represents  $\log_2(\text{Fold-change})$  of 0.375 (FC=1.3) and FDR<0.1 that was used as the cell type-  
1403 specificity enrichment cutoff. Asterisks denote genes in IOP loci not associated with POAG risk (**h**).  
1404 **f-g**, Heatmap of fraction of genes that overlap between the e/sGenes driving the enrichment signal  
1405 for top ranked cell types ( $P<0.05$ ) in the anterior segment for POAG cross-ancestry (**f**) and IOP (**g**)  
1406 GWAS loci. Numbers refer to the fraction of e/sGenes driving the cell type enrichment on each row  
1407 that overlaps with the genes driving the cell type enrichment on the corresponding column.  
1408 Hierarchical clustering was performed on both rows and columns using the euclidean distance  
1409 between fractions. Red asterisks: tissue-wide BH FDR<0.1. **i**, Bubble map displaying the  
1410 expression of the e/sGenes driving the IOP enrichment in pericytes across all cell types in the  
1411 anterior segment. The colorbar represents gene expression z-scores computed by comparing each  
1412 gene's average expression in a given cell type to its per cell type average expression across all  
1413 types divided by the standard deviation of all cell type expression averages. Bubble size is  
1414 proportional to the percentage of cells expressing the given gene ( $\log(\text{TPK}+1)>1$ ). Cell type  
1415 abbreviations are described in Supplementary Table 38.

1416

1417

1418

**Figure 7**



1452 **Figure 7. Cell type enrichment of e/sQTL-mapped genes for POAG, IOP and related trait loci**  
1453 **in retina, optic nerve head and surrounding tissues.** **a,b**, Significance (circle size,  $-\log_{10}(P$ -  
1454 value)) and fold-enrichment (circle color) of the cell type specificity of GWAS locus sets for POAG  
1455 cross-ancestry, POAR European subset, IOP, and physician (VCDR) and machine learning (ML)-  
1456 defined VCDR (VCDR<sub>ML</sub>\_Alipanahi) are shown for each of the 15 cell types found in retina **(a)**  
1457 and 36 cell types in optic nerve head (ONH), optic nerve (ON), peripapillary sclera, sclera and  
1458 choroid **(b)**. Traits (rows) and cell types (columns) were clustered based on hierarchical clustering  
1459 of the euclidean distance between GWAS locus set cell type-specificity enrichment scores. Red  
1460 rings: experiment-wide significant (BH FDR<0.1); Yellow rings: tissue-wide significant (BH  
1461 FDR<0.1); Grey rings: nominal significant ( $P<0.05$ ). **c**, Cell type specificity fold-enrichment (x-axis)  
1462 in the ONH and surrounding tissue cell types ranked in descending order for the POAG cross-  
1463 ancestry GWAS locus set. **d**, Differential expression ( $\log_2(\text{Fold-change})$ ) in astrocytes, the most  
1464 strongly enriched cell type for POAG cross-ancestry GWAS loci in the ONH, compared to all other  
1465 cell types in the posterior tissues is shown for the set of genes driving the POAG enrichment signal  
1466 in astrocytes. Horizontal dashed line represents  $\log_2(\text{Fold-change})$  of 0.375 (FC=1.3) and FDR<0.1  
1467 that was used as the cell type-specificity enrichment cutoff. **e**, The expression profile of the  
1468 e/sGenes driving the POAG cross-ancestry enrichment signal in astrocytes is shown across all cell  
1469 types in the ONH and surrounding tissues. Color represents z-scores computed by comparing each  
1470 gene's average expression in a given cell type to the average expression across all cell types  
1471 divided by its standard deviation of all cell type expression averages. Bubble size is proportional to  
1472 the percentage of cells expressing the gene ( $\log(\text{TPK}+1)>1$ ). **f**, LocusCompare plot of  $-\log_{10}(P$ -  
1473 value) of the POAG cross-ancestry GWAS meta-analysis relative to  $-\log_{10}(P\text{-value})$  of a retina eQTL  
1474 acting on *DGKG* that significantly colocalized with the POAG GWAS locus rs56233426  
1475 (chr3\_186411027\_G\_A). *DGKG* is the strongest astrocyte-specific gene driving the cell type  
1476 enrichment signal for POAG loci. Points are color-coded based on LD ( $r^2$ ) relative to the eVariant  
1477 with the highest colocalization posterior probability (CLPP=0.93). The red arrow is pointing to the  
1478 lead POAG GWAS variant. Cell type abbreviations are described in Supplementary Table 38.

1479 **Table 1. List of high-confidence colocalizing expression and splicing QTLs with POAG and**  
 1480 **IOP GWAS loci.**

GWAS locus	RS ID	GWAS effect (OR or beta)	# e/sGenes tested per locus	# significantly colocalizing e/sGenes with eCAVIAR or enloc			Significantly colocalizing e/sGenes with eCAVIAR and enloc and significant with MR	Nearest Gene	Significant in GWAS:	
				eCAVIAR	enloc	GWAS			IOP	POAG European
POAG cross-ancestry GWAS										
chr1:171636338:G:A	rs74315329	5.46957	24	1		<i>PIGC</i> (s)	-	-	-	-
chr1:165768467:G:C	rs2790053	1.35026	13	2		<i>TMCO1</i> (e,s)	-	+	<i>TMCO1</i>	<i>TMCO1</i>
chr9:22051671:G:C	rs944801	1.2663	26	3		<i>CDKN2B-AS1</i> (s)	-	+	-	<i>CDKN2B-AS1</i>
chr4:7902636:G:A	rs938604	0.866407	27	2		<i>AFAP1</i> (e)	-	+	<i>AFAP1</i>	-
chr17:10127866:G:A	rs9913911	1.14912	30	1		<i>GAS7</i> (e)	-	+	<i>GAS7</i>	<i>GAS7</i>
chr9:126628521:C:T	rs3829849	0.87529	11	4		<i>LMX1B</i> (e)	-	+	<i>LMX1B</i>	<i>LMX1B</i>
chr7:116522522:T:A	rs10257125	0.890921	18	2		<i>CAV2</i> (e,s)	-	-	<i>CAV2</i>	<i>CAV2</i>
chr11:86657064:C:T	rs10792871	1.12142	15	4		<i>PRSS23</i> (e), <i>ME3</i> (e)	-	+	<i>PRSS23, ME3</i>	<i>PRSS23, ME3</i>
chr9:133255801:C:T	rs8176749	1.10186	18	1		<i>ABO</i> (e)	-	+	<i>ABO</i>	-
chr15:73928957:C:T	rs1550437	0.913657	72	2		<i>LOXL1</i> (e,s)	-	+	-	<i>LOXL1</i>
chr3:188349156:G:T	rs6787621	0.92626	7	1		<i>LPP</i> (e,s)	-	+	<i>LPP</i>	-
chr22:28712241:G:A	rs5752776	0.926631	27	5		<i>TTC28</i> (e)	-	+	-	<i>TTC28</i>
chr2:12811195:C:T	rs12623251	0.932021	11	1		<i>TRIB2</i> (e)	-	+	-	<i>TRIB2</i>
chr15:57261634:T:A	rs2431023	1.07026	16	2		<i>ZNF280D</i> (e), <i>TCF12</i> (e)	-	+	-	<i>ZNF280D, TCF12</i>
chr11:130412183:C:T	rs2875238	0.935289	7	2		<i>RP11-122M12.1</i> (e,s), <i>ADAMTS8</i> (e)	-	+	-	-
chr7:134835770:C:A	rs10237321	0.94535	29	1		<i>CALD1</i> (e)	-	+	-	-
chr6:134051012:G:C	rs2811688	0.946296	3	3		<i>SLC2A12</i> (e), <i>TBPL1</i> (e)	<i>SLC2A12</i>	+	-	<i>SLC2A12, TBPL1</i>
IOP GWAS										
chr1:165715441:C:T	rs116089225	-0.744	29	3		<i>TMCO1</i> (e)	-	+	<i>TMCO1</i>	<i>TMCO1</i>
chr14:74498200:C:T	rs74384554	0.417	70	4		<i>NPC2</i> (e)	<i>NPC2</i>	-	-	<i>NPC2</i>
chr17:10127866:G:A	rs9913911	0.231	3	1		<i>GAS7</i> (e)	-	+	<i>GAS7</i>	<i>GAS7</i>
chr7:116511284:C:T	rs10281637	-0.225	13	3		<i>CAV2</i> (e), <i>CAV1</i> (e)	-	+	<i>CAV2</i>	<i>CAV2</i>
chr11:12042249:G:A	rs11217863	-0.224	17	2		<i>ARHGEF12</i> (e,s)	-	+	<i>ARHGEF12</i>	<i>ARHGEF12</i>
chr1:218937686:C	rs7310335	0.206	11	2		<i>LYPLAL1-AS1</i> (e,s)	-	+	-	-
chr5:108710999:G:A	rs73220177	0.165	9	2		<i>LINC01023</i> (e)	-	-	-	-
chr2:19854787:G:A	rs17534001	0.16	26	4		<i>TXNRD2</i> (e,s)	-	+	<i>TXNRD2</i>	<i>TXNRD2</i>
chr6:170146547:G:T	rs59020521	-0.148	18	2		<i>RP11-302L19.3</i> (e)	-	-	-	<i>RP11-302L19.3</i>
chr2:29224336:C:A	rs9608740	-0.141	40	3		<i>EMID1</i> (e,s)	-	+	<i>EMID1</i>	-
chr2:238402728:C:T	rs57435966	0.132	25	3		<i>TRAF3IP1</i> (e)	-	+	-	-
chr11:16988629:C:A	rs4141194	-0.131	18	5		<i>NCR3LG1</i> (e), <i>KCNJ11</i> (e,s), <i>NUCB2</i> (s)	<i>NCR3LG1</i>	-	-	<i>NUCB2</i>
chr11:86699199:C:T	rs2433414	-0.128	22	6		<i>ME3</i> (e)	-	+	<i>ME3</i>	<i>ME3</i>
chr11:47253513:G:A	rs10838681	-0.124	56	12		<i>PTPRJ</i> (e)	-	-	-	-
chr3:50162314:G:A	rs11710277	-0.12	117	14		<i>LSMEM2</i> (e)	-	-	-	-
chr15:61659036:C:T	rs4775427	-0.111	7	5		<i>RP11-507B12.1</i> (e), <i>RP11-507B12.2</i> (e), <i>RP11-162I.1</i> (e)	-	-	<i>RP11-507B12.1, RP11-507B12.2, RP11-162I.1</i>	<i>RP11-507B12.1, RP11-507B12.2, RP11-162I.1</i>
chr14:52920118:G:C	rs8009633	0.11	12	2		<i>FERMT2</i> (e,s)	-	+	-	-
chr2:101031432:G:A	rs55771809	0.109	17	3		<i>TBC1D8</i> (s)	<i>TBC1D8</i>	+	-	-
chr7:116171382:C:A	rs2896175	0.108	12	4		<i>TES</i> (e)	-	-	-	-
chr16:89752083:C:T	rs3743860	0.102	57	14		<i>ZNF276</i> (e,s), <i>SPIRE2</i> (e), <i>FANCA</i> (e,s), <i>VPS9D1</i> (e)	-	+	-	-
chr11:78374959:C:T	rs10793308	0.098	25	4		<i>NARS2</i> (e,s), <i>USP35</i> (e)	-	-	-	-
chr11:86789159:C:T	rs11606902	-0.098	12	4		<i>PRSS23</i> (e), <i>ME3</i> (e)	<i>PRSS23</i>	+	<i>PRSS23, ME3</i>	<i>PRSS23, ME3</i>
chr11:12639117:G:C	rs61818802	-0.097	14	4		<i>MOV10</i> (e), <i>RHOC</i> (e)	-	-	-	<i>MOV10</i>
chr3:50143702:G:T	rs2526385	0.096	116	16		<i>LSMEM2</i> (e)	-	-	-	-
chr22:3778844:C:T	rs6000889	0.094	47	10		<i>GCAT</i> (e,s)	-	-	-	<i>GCAT</i>
chr7:11644065:C:T	rs1635182	-0.094	4	1		<i>THSD7A</i> (e)	-	+	-	<i>THSD7A</i>
chr3:188343926:C:T	rs4132172	0.093	4	2		<i>LPP</i> (e,s)	-	+	-	<i>LPP</i>
chr17:46758936:C:T	rs9912530	0.091	58	14		<i>WNT3</i> (e)	-	+	<i>WNT3</i>	-
chr1:37627051:C:T	rs4074961	-0.089	17	5		<i>GNL2</i> (e,s), <i>MEAF6</i> (e), <i>DNAL1</i> (s)	<i>MEAF6</i>	-	<i>GNL2, MEAF6, DNAL1</i>	-
chr10:80411803:C:T	rs6585986	-0.084	37	4		<i>TSPAN14</i> (s), <i>ANXA11</i> (e)	-	-	-	-
chr13:75683130:G:C	rs9544022	-0.081	9	2		<i>LMO7</i> (s)	-	+	<i>LMO7</i>	-
chr2:217802649:T:A	rs3791979	-0.081	9	2		<i>TNS1</i> (e,s)	-	+	-	-
chr11:817786:C:T	rs10902223	0.079	49	18		<i>PIDD1, CRACR2B, PNPLA2, CHID1</i>	-	-	-	-
chr10:92670768:G:A	rs9419741	-0.077	19	4		<i>HHEX</i> (e)	-	+	-	-
chr1:31726197:G:C	rs945211	-0.073	28	5		<i>COL16A1</i> (e,s)	-	-	-	-
chr6:39895441:G:A	rs3004063	0.071	9	3		<i>MOC31</i> (e), <i>RP11-61I13.3</i> (e,s), <i>DAAM2</i> (s)	-	+	-	-
chr17:49264218:C:T	rs9899665	-0.069	31	2		<i>GNGT2</i> (e)	-	-	-	-

1481  
 1482 Table lists target genes of expression and splicing QTLs (e/sGenes) that were significant based  
 1483 on colocalization analysis with both eCAVIAR (CLPP>0.01) and enloc (RCP>0.1) and Mendelian  
 1484 Randomization (MR) analysis (FDR<0.05) for POAG and/or IOP GWAS loci.

1486 **References**

- 1487 1. Tham, Y.-C. *et al.* Global prevalence of glaucoma and projections of glaucoma burden  
1488 through 2040: a systematic review and meta-analysis. *Ophthalmology* **121**, 2081–2090  
1489 (2014).
- 1490 2. Weinreb, R. N. *et al.* Primary open-angle glaucoma. *Nat Rev Dis Primers* **2**, 16067 (2016).
- 1491 3. Leske, M. C. *et al.* Predictors of long-term progression in the early manifest glaucoma trial.  
1492 *Ophthalmology* **114**, 1965–1972 (2007).
- 1493 4. Kwon, Y. H., Fingert, J. H., Kuehn, M. H. & Alward, W. L. M. Primary open-angle glaucoma.  
1494 *N. Engl. J. Med.* **360**, 1113–1124 (2009).
- 1495 5. Kim, J. *et al.* Impaired angiopoietin/Tie2 signaling compromises Schlemm's canal integrity  
1496 and induces glaucoma. *J. Clin. Invest.* **127**, 3877–3896 (2017).
- 1497 6. Costagliola, C. *et al.* How many aqueous humor outflow pathways are there? *Surv.*  
1498 *Ophthalmol.* **65**, 144–170 (2020).
- 1499 7. Anderson, D. R., Drance, S. M., Schulzer, M. & Collaborative Normal-Tension Glaucoma  
1500 Study Group. Natural history of normal-tension glaucoma. *Ophthalmology* **108**, 247–253  
1501 (2001).
- 1502 8. Gharakhani, P. *et al.* Genome-wide meta-analysis identifies 127 open-angle glaucoma loci  
1503 with consistent effect across ancestries. *Nat. Commun.* **12**, 1258 (2021).
- 1504 9. Khawaja, A. P. *et al.* Genome-wide analyses identify 68 new loci associated with intraocular  
1505 pressure and improve risk prediction for primary open-angle glaucoma. *Nature Genetics* vol.  
1506 50 778–782 Preprint at <https://doi.org/10.1038/s41588-018-0126-8> (2018).
- 1507 10. MacGregor, S. *et al.* Genome-wide association study of intraocular pressure uncovers new  
1508 pathways to glaucoma. *Nature Genetics* vol. 50 1067–1071 Preprint at  
1509 <https://doi.org/10.1038/s41588-018-0176-y> (2018).
- 1510 11. Gao, X. R. *et al.* Genome-wide association analyses identify new loci influencing intraocular  
1511 pressure. *Human Molecular Genetics* vol. 27 2205–2213 Preprint at  
1512 <https://doi.org/10.1093/hmg/ddy111> (2018).
- 1513 12. Alipanahi, B. *et al.* Large-scale machine-learning-based phenotyping significantly improves  
1514 genomic discovery for optic nerve head morphology. *Am. J. Hum. Genet.* **108**, 1217–1230  
1515 (2021).
- 1516 13. Springelkamp, H. *et al.* New insights into the genetics of primary open-angle glaucoma  
1517 based on meta-analyses of intraocular pressure and optic disc characteristics. *Hum. Mol.*  
1518 *Genet.* **26**, 438–453 (2017).

- 1519 14. Lu, Y. *et al.* Common genetic variants near the Brittle Cornea Syndrome locus ZNF469  
1520 influence the blinding disease risk factor central corneal thickness. *PLoS Genet.* **6**,  
1521 e1000947 (2010).
- 1522 15. Vitart, V. *et al.* New loci associated with central cornea thickness include COL5A1, AKAP13  
1523 and AVGR8. *Hum. Mol. Genet.* **19**, 4304–4311 (2010).
- 1524 16. Hoehn, R. *et al.* Population-based meta-analysis in Caucasians confirms association with  
1525 COL5A1 and ZNF469 but not COL8A2 with central corneal thickness. *Hum. Genet.* **131**,  
1526 1783–1793 (2012).
- 1527 17. Gao, X. *et al.* A genome-wide association study of central corneal thickness in Latinos.  
1528 *Invest. Ophthalmol. Vis. Sci.* **54**, 2435–2443 (2013).
- 1529 18. Iglesias, A. I. *et al.* Cross-ancestry genome-wide association analysis of corneal thickness  
1530 strengthens link between complex and Mendelian eye diseases. *Nat. Commun.* **9**, 1864  
1531 (2018).
- 1532 19. Gao, X. *et al.* Genome-wide association study identifies WNT7B as a novel locus for central  
1533 corneal thickness in Latinos. *Hum. Mol. Genet.* **25**, 5035–5045 (2016).
- 1534 20. Fan, B. J. *et al.* Family-Based Genome-Wide Association Study of South Indian Pedigrees  
1535 Supports WNT7B as a Central Corneal Thickness Locus. *Invest. Ophthalmol. Vis. Sci.* **59**,  
1536 2495–2502 (2018).
- 1537 21. Ivarsdottir, E. V. *et al.* Sequence variation at ANAPC1 accounts for 24% of the variability in  
1538 corneal endothelial cell density. *Nat. Commun.* **10**, 1284 (2019).
- 1539 22. Simcoe, M. J., Khawaja, A. P., Hysi, P. G., Hammond, C. J. & UK Biobank Eye and Vision  
1540 Consortium. Genome-wide association study of corneal biomechanical properties identifies  
1541 over 200 loci providing insight into the genetic etiology of ocular diseases. *Hum. Mol. Genet.*  
1542 **29**, 3154–3164 (2020).
- 1543 23. Han, X. *et al.* Automated AI labeling of optic nerve head enables insights into cross-ancestry  
1544 glaucoma risk and genetic discovery in >280,000 images from UKB and CLSA. *Am. J. Hum.*  
1545 *Genet.* **108**, 1204–1216 (2021).
- 1546 24. Gamazon, E. R. *et al.* Using an atlas of gene regulation across 44 human tissues to inform  
1547 complex disease- and trait-associated variation. *Nat. Genet.* **50**, 956–967 (2018).
- 1548 25. Finucane, H. K. *et al.* Heritability enrichment of specifically expressed genes identifies  
1549 disease-relevant tissues and cell types. *Nat. Genet.* **50**, 621–629 (2018).
- 1550 26. GTEx Consortium. The GTEx Consortium atlas of genetic regulatory effects across human  
1551 tissues. *Science* **369**, 1318–1330 (2020).

- 1552 27. Ratnapriya, R. *et al.* Retinal transcriptome and eQTL analyses identify genes associated  
1553 with age-related macular degeneration. *Nat. Genet.* **51**, 606–610 (2019).
- 1554 28. Strunz, T. *et al.* A mega-analysis of expression quantitative trait loci in retinal tissue. *PLoS*  
1555 *Genet.* **16**, e1008934 (2020).
- 1556 29. Orozco, L. D. *et al.* Integration of eQTL and a single-cell atlas in the human eye identifies  
1557 causal genes for age-related macular degeneration. *Cell Rep.* **30**, 1246-1259.e6 (2020).
- 1558 30. Liu, B. *et al.* Genetic analyses of human fetal retinal pigment epithelium gene expression  
1559 suggest ocular disease mechanisms. *Commun. Biol.* **2**, 186 (2019).
- 1560 31. Yan, W. *et al.* Cell Atlas of The Human Fovea and Peripheral Retina. *Sci. Rep.* **10**, 9802  
1561 (2020).
- 1562 32. Dharmat, R., Kim, S., Li, Y. & Chen, R. Single-Cell Capture, RNA-seq, and Transcriptome  
1563 Analysis from the Neural Retina. *Methods Mol. Biol.* **2092**, 159–186 (2020).
- 1564 33. Liang, Q. *et al.* A multi-omics atlas of the human retina at single-cell resolution. *Cell Genom.*  
1565 **3**, 100298 (2023).
- 1566 34. van Zyl, T. *et al.* Cell atlas of aqueous humor outflow pathways in eyes of humans and four  
1567 model species provides insight into glaucoma pathogenesis. *Proc. Natl. Acad. Sci. U. S. A.*  
1568 **117**, 10339–10349 (2020).
- 1569 35. Patel, G. *et al.* Molecular taxonomy of human ocular outflow tissues defined by single-cell  
1570 transcriptomics. *Proc. Natl. Acad. Sci. U. S. A.* **117**, 12856–12867 (2020).
- 1571 36. van Zyl, T. *et al.* Cell atlas of the human ocular anterior segment: Tissue-specific and shared  
1572 cell types. *Proc. Natl. Acad. Sci. U. S. A.* **119**, e2200914119 (2022).
- 1573 37. Monavarfeshani, A. *et al.* Transcriptomic Analysis of the Ocular Posterior Segment  
1574 Completes a Cell Atlas of the Human Eye. *bioRxiv* (2023) doi:10.1101/2023.04.26.538447.
- 1575 38. Eraslan, G. *et al.* Single-nucleus cross-tissue molecular reference maps toward  
1576 understanding disease gene function. *Science* **376**, eabl4290 (2022).
- 1577 39. Rouhana, J., J. Wang, G. Eraslan, S. Anand, A. Hamel, B. Cole, A. Regev, F. Aguet, K.  
1578 Ardlie, and A. V. Segrè. ECLIPSER: identifying causal cell types and genes for complex  
1579 traits through single cell enrichment of e/sQTL-mapped genes in GWAS loci. *BioRxiv* (2021)  
1580 doi:10.1101/2021.11.24.469720.
- 1581 40. Marchal, C. *et al.* High-resolution genome topology of human retina uncovers super  
1582 enhancer-promoter interactions at tissue-specific and multifactorial disease loci. *Nat.*  
1583 *Commun.* **13**, 5827 (2022).
- 1584 41. Hormozdiari, F. *et al.* Colocalization of GWAS and eQTL Signals Detects Target Genes. *Am.*  
1585 *J. Hum. Genet.* **99**, 1245–1260 (2016).

- 1586 42. Wen, X., Pique-Regi, R. & Luca, F. Integrating molecular QTL data into genome-wide  
1587 genetic association analysis: Probabilistic assessment of enrichment and colocalization.  
1588 *PLoS Genet.* **13**, e1006646 (2017).
- 1589 43. Thomson, B. R. *et al.* Angiopoietin-1 is required for Schlemm's canal development in mice  
1590 and humans. *J. Clin. Invest.* **127**, 4421–4436 (2017).
- 1591 44. Wiggs, J. L. *et al.* Common variants at 9p21 and 8q22 are associated with increased  
1592 susceptibility to optic nerve degeneration in glaucoma. *PLoS Genet.* **8**, e1002654 (2012).
- 1593 45. Collantes, E. R. A. *et al.* EFEMP1 rare variants cause familial juvenile-onset open-angle  
1594 glaucoma. *Hum. Mutat.* **43**, 240–252 (2022).
- 1595 46. Wiggs, J. L. & Pasquale, L. R. Genetics of glaucoma. *Hum. Mol. Genet.* **26**, R21–R27  
1596 (2017).
- 1597 47. Lewczuk, K., Jabłońska, J., Konopińska, J., Mariak, Z. & Rękas, M. Schlemm's canal: the  
1598 outflow "vessel." *Acta Ophthalmol.* (2021) doi:10.1111/aos.15027.
- 1599 48. Barbeira, A. N. *et al.* Exploiting the GTEx resources to decipher the mechanisms at GWAS  
1600 loci. *Genome Biol.* **22**, 49 (2021).
- 1601 49. Zhu, Z. *et al.* Integration of summary data from GWAS and eQTL studies predicts complex  
1602 trait gene targets. *Nat. Genet.* **48**, 481–487 (2016).
- 1603 50. Hemani, G., Bowden, J. & Davey Smith, G. Evaluating the potential role of pleiotropy in  
1604 Mendelian randomization studies. *Hum. Mol. Genet.* **27**, R195–R208 (2018).
- 1605 51. Zuber, V. *et al.* Combining evidence from Mendelian randomization and colocalization:  
1606 Review and comparison of approaches. *Am. J. Hum. Genet.* **109**, 767–782 (2022).
- 1607 52. Hukku, A. *et al.* Probabilistic colocalization of genetic variants from complex and molecular  
1608 traits: promise and limitations. *Am. J. Hum. Genet.* **108**, 25–35 (2021).
- 1609 53. Wallace, C. Eliciting priors and relaxing the single causal variant assumption in  
1610 colocalisation analyses. *PLoS Genet.* **16**, e1008720 (2020).
- 1611 54. GTEx Consortium *et al.* Genetic effects on gene expression across human tissues. *Nature*  
1612 **550**, 204–213 (2017).
- 1613 55. Claussnitzer, M. *et al.* FTO Obesity Variant Circuitry and Adipocyte Browning in Humans. *N.  
1614 Engl. J. Med.* **373**, 895–907 (2015).
- 1615 56. Nasser, J. *et al.* Genome-wide enhancer maps link risk variants to disease genes. *Nature*  
1616 **593**, 238–243 (2021).
- 1617 57. Cao, J. *et al.* Joint profiling of chromatin accessibility and gene expression in thousands of  
1618 single cells. *Science* **361**, 1380–1385 (2018).

- 1619 58. Mackay, D. S., Bennett, T. M. & Shiels, A. Exome Sequencing Identifies a Missense Variant  
1620 in EFEMP1 Co-Segregating in a Family with Autosomal Dominant Primary Open-Angle  
1621 Glaucoma. *PLoS One* **10**, e0132529 (2015).
- 1622 59. Lim, S.-H. *et al.* CYP1B1, MYOC, and LTBP2 mutations in primary congenital glaucoma  
1623 patients in the United States. *Am. J. Ophthalmol.* **155**, 508-517.e5 (2013).
- 1624 60. Fuchshofer, R. & Tamm, E. R. The role of TGF- $\beta$  in the pathogenesis of primary open-angle  
1625 glaucoma. *Cell Tissue Res.* **347**, 279–290 (2012).
- 1626 61. Scerbo, P. & Monsoro-Burq, A. H. The vertebrate-specific VENTX/NANOG gene empowers  
1627 neural crest with ectomesenchyme potential. *Sci Adv* **6**, eaaz1469 (2020).
- 1628 62. Kumar, S., Kumar, V., Li, W. & Kim, J. Ventx Family and Its Functional Similarities with  
1629 Nanog: Involvement in Embryonic Development and Cancer Progression. *Int. J. Mol. Sci.* **23**,  
1630 (2022).
- 1631 63. Fadini, G. P. *et al.* Reduced endothelial progenitor cells and brachial artery flow-mediated  
1632 dilation as evidence of endothelial dysfunction in ocular hypertension and primary open-  
1633 angle glaucoma. *Acta Ophthalmol.* **88**, 135–141 (2010).
- 1634 64. Su, W.-W. *et al.* Glaucoma is associated with peripheral vascular endothelial dysfunction.  
1635 *Ophthalmology* **115**, 1173-1178.e1 (2008).
- 1636 65. Green, K. J., Getsios, S., Troyanovsky, S. & Godsel, L. M. Intercellular junction assembly,  
1637 dynamics, and homeostasis. *Cold Spring Harb. Perspect. Biol.* **2**, a000125 (2010).
- 1638 66. Pattabiraman, P. P., Epstein, D. L. & Rao, P. V. Regulation of Adherens Junctions in  
1639 Trabecular Meshwork Cells by Rac GTPase and their influence on Intraocular Pressure. *J.*  
1640 *Ocul. Biol. Dis. Infor.* **1**, (2013).
- 1641 67. Gould, D. B., Smith, R. S. & John, S. W. M. Anterior segment development relevant to  
1642 glaucoma. *Int. J. Dev. Biol.* **48**, 1015–1029 (2004).
- 1643 68. Ronen E. Mukamel, Robert E. Handsaker, Maxwell A. Sherman, Alison R. Barton, Margaux  
1644 L. A. Hujoel, Steven A. McCarroll, Po-Ru Loh. Repeat polymorphisms in non-coding DNA  
1645 underlie top genetic risk loci for glaucoma and colorectal cancer. *bioRxiv* (2022)  
1646 doi:10.1101/2022.10.11.22280955.
- 1647 69. Pasquale, L. R. *et al.* CDKN2B-AS1 genotype-glaucoma feature correlations in primary  
1648 open-angle glaucoma patients from the United States. *Am. J. Ophthalmol.* **155**, 342-353.e5  
1649 (2013).
- 1650 70. Kim, B. J. & Scott, D. A. RERE deficiency causes retinal and optic nerve atrophy through  
1651 degeneration of retinal cells. *Dev. Dyn.* **250**, 1398–1409 (2021).

- 1652 71. Wang, H. *et al.* Physiological function of myocilin and its role in the pathogenesis of  
1653 glaucoma in the trabecular meshwork (Review). *Int. J. Mol. Med.* **43**, 671–681 (2019).
- 1654 72. Finucane, H. K. *et al.* Partitioning heritability by functional annotation using genome-wide  
1655 association summary statistics. *Nat. Genet.* **47**, 1228–1235 (2015).
- 1656 73. Watanabe, K., Taskesen, E., van Bochoven, A. & Posthuma, D. Functional mapping and  
1657 annotation of genetic associations with FUMA. *Nat. Commun.* **8**, 1826 (2017).
- 1658 74. Jagadeesh, K. A. *et al.* Identifying disease-critical cell types and cellular processes across  
1659 the human body by integration of single-cell profiles and human genetics. *bioRxiv*  
1660 2021.03.19.436212 (2021) doi:10.1101/2021.03.19.436212.
- 1661 75. Slowikowski, K., Hu, X. & Raychaudhuri, S. SNPsea: an algorithm to identify cell types,  
1662 tissues and pathways affected by risk loci. *Bioinformatics* **30**, 2496–2497 (2014).
- 1663 76. Calderon, D. *et al.* Inferring Relevant Cell Types for Complex Traits by Using Single-Cell  
1664 Gene Expression. *Am. J. Hum. Genet.* **101**, 686–699 (2017).
- 1665 77. Stamer, W. D. & Acott, T. S. Current understanding of conventional outflow dysfunction in  
1666 glaucoma. *Curr. Opin. Ophthalmol.* **23**, 135–143 (2012).
- 1667 78. Alarcon-Martinez, L. *et al.* Pericyte dysfunction and loss of interpericyte tunneling nanotubes  
1668 promote neurovascular deficits in glaucoma. *Proc. Natl. Acad. Sci. U. S. A.* **119**, (2022).
- 1669 79. Wang, R., Seifert, P. & Jakobs, T. C. Astrocytes in the Optic Nerve Head of Glaucomatous  
1670 Mice Display a Characteristic Reactive Phenotype. *Invest. Ophthalmol. Vis. Sci.* **58**, 924–  
1671 932 (2017).
- 1672 80. Zhao, X., Sun, R., Luo, X., Wang, F. & Sun, X. The Interaction Between Microglia and  
1673 Macroglia in Glaucoma. *Front. Neurosci.* **15**, 610788 (2021).
- 1674 81. Shinozaki, Y. & Koizumi, S. Potential roles of astrocytes and Müller cells in the pathogenesis  
1675 of glaucoma. *J. Pharmacol. Sci.* **145**, 262–267 (2021).
- 1676 82. Tovar-Vidales, T., Wordinger, R. J. & Clark, A. F. Identification and localization of lamina  
1677 cribrosa cells in the human optic nerve head. *Exp. Eye Res.* **147**, 94–97 (2016).
- 1678 83. Lopez, N. N., Clark, A. F. & Tovar-Vidales, T. Isolation and characterization of human optic  
1679 nerve head astrocytes and lamina cribrosa cells. *Exp. Eye Res.* **197**, 108103 (2020).
- 1680 84. Strickland, R. G., Garner, M. A., Gross, A. K. & Girkin, C. A. Remodeling of the lamina  
1681 cribrosa: Mechanisms and potential therapeutic approaches for glaucoma. *Int. J. Mol. Sci.*  
1682 **23**, 8068 (2022).
- 1683 85. Calkins, D. J. Critical pathogenic events underlying progression of neurodegeneration in  
1684 glaucoma. *Prog. Retin. Eye Res.* **31**, 702–719 (2012).

- 1685 86. Venkataraman, S. T., Flanagan, J. G. & Hudson, C. Vascular reactivity of optic nerve head  
1686 and retinal blood vessels in glaucoma--a review. *Microcirculation* **17**, 568–581 (2010).
- 1687 87. Tamm, E. R., Ethier, C. R. & Lasker/IRRF Initiative on Astrocytes and Glaucomatous  
1688 Neurodegeneration Participants. Biological aspects of axonal damage in glaucoma: A brief  
1689 review. *Exp. Eye Res.* **157**, 5–12 (2017).
- 1690 88. Paula, J. S., O'Brien, C. & Stamer, W. D. Life under pressure: The role of ocular cribiform  
1691 cells in preventing glaucoma. *Exp. Eye Res.* **151**, 150–159 (2016).
- 1692 89. Zeng, H.-L. & Shi, J.-M. The role of microglia in the progression of glaucomatous  
1693 neurodegeneration- a review. *Int. J. Ophthalmol.* **11**, 143–149 (2018).
- 1694 90. Kim-Hellmuth, S., Aguet, F. & Oliva, M. Cell type–specific genetic regulation of gene  
1695 expression across human tissues. (2020).
- 1696 91. van der Wijst, M. *et al.* The single-cell eQTLGen consortium. *Elife* **9**, (2020).
- 1697 92. Li, Y. I. *et al.* Annotation-free quantification of RNA splicing using LeafCutter. *Nat. Genet.* **50**,  
1698 151–158 (2018).
- 1699 93. Pruim, R. J. *et al.* LocusZoom: regional visualization of genome-wide association scan  
1700 results. *Bioinformatics* **26**, 2336–2337 (2010).
- 1701 94. Storey, J. D. & Tibshirani, R. Statistical significance for genomewide studies. *Proc. Natl.*  
1702 *Acad. Sci. U. S. A.* **100**, 9440–9445 (2003).
- 1703 95. Gamazon, E. R., Huang, R. S., Dolan, M. E., Cox, N. J. & Im, H. K. Integrative genomics:  
1704 quantifying significance of phenotype-genotype relationships from multiple sources of high-  
1705 throughput data. *Front. Genet.* **3**, 202 (2012).
- 1706 96. Zheng-Bradley, X. *et al.* Alignment of 1000 Genomes Project reads to reference assembly  
1707 GRCh38. *Gigascience* **6**, 1–8 (2017).
- 1708 97. Smith, G. D. & Ebrahim, S. “Mendelian randomization”: can genetic epidemiology contribute  
1709 to understanding environmental determinants of disease? *Int. J. Epidemiol.* **32**, 1–22 (2003).
- 1710 98. Yavorska, O. O. & Burgess, S. MendelianRandomization: an R package for performing  
1711 Mendelian randomization analyses using summarized data. *Int. J. Epidemiol.* **46**, 1734–1739  
1712 (2017).
- 1713 99. Burgess, S., Small, D. S. & Thompson, S. G. A review of instrumental variable estimators for  
1714 Mendelian randomization. *Stat. Methods Med. Res.* **26**, 2333–2355 (2017).
- 1715 100. Burgess, S., Butterworth, A. & Thompson, S. G. Mendelian randomization analysis with  
1716 multiple genetic variants using summarized data. *Genet. Epidemiol.* **37**, 658–665 (2013).

- 1717 101. Bowden, J., Davey Smith, G., Haycock, P. C. & Burgess, S. Consistent Estimation in  
1718 Mendelian Randomization with Some Invalid Instruments Using a Weighted Median  
1719 Estimator. *Genet. Epidemiol.* **40**, 304–314 (2016).
- 1720 102. Bowden, J., Davey Smith, G. & Burgess, S. Mendelian randomization with invalid  
1721 instruments: effect estimation and bias detection through Egger regression. *Int. J. Epidemiol.*  
1722 **44**, 512–525 (2015).
- 1723 103. Verbanck, M., Chen, C.-Y., Neale, B. & Do, R. Detection of widespread horizontal pleiotropy  
1724 in causal relationships inferred from Mendelian randomization between complex traits and  
1725 diseases. *Nat. Genet.* **50**, 693–698 (2018).
- 1726 104. Quinlan, A. R. BEDTools: The Swiss-army tool for genome feature analysis. *Curr. Protoc.*  
1727 *Bioinformatics* **47**, 11.12.1-34 (2014).
- 1728 105. Finak, G. *et al.* MAST: a flexible statistical framework for assessing transcriptional changes  
1729 and characterizing heterogeneity in single-cell RNA sequencing data. *Genome Biol.* **16**, 278  
1730 (2015).
- 1731 106. Ghoussaini, M. *et al.* Open Targets Genetics: systematic identification of trait-associated  
1732 genes using large-scale genetics and functional genomics. *Nucleic Acids Res.* **49**, D1311–  
1733 D1320 (2021).
- 1734 107. Watanabe, K., Umićević Mirkov, M., de Leeuw, C. A., van den Heuvel, M. P. & Posthuma, D.  
1735 Genetic mapping of cell type specificity for complex traits. *Nat. Commun.* **10**, 3222 (2019).
- 1736 108. de Leeuw, C. A., Mooij, J. M., Heskes, T. & Posthuma, D. MAGMA: generalized gene-set  
1737 analysis of GWAS data. *PLoS Comput. Biol.* **11**, e1004219 (2015).
- 1738 109. Pollack, S. *et al.* Multiethnic Genome-Wide Association Study of Diabetic Retinopathy Using  
1739 Liability Threshold Modeling of Duration of Diabetes and Glycemic Control. *Diabetes* **68**,  
1740 441–456 (2019).
- 1741 110. Li, B. & Dewey, C. N. RSEM: accurate transcript quantification from RNA-Seq data with or  
1742 without a reference genome. *BMC Bioinformatics* **12**, 323 (2011).